TKK Dissertations 153
Espoo 2009

VERY LOW NOISE CRYOGENIC RECEIVERS AND MEASUREMENT ELECTRONICS

Doctoral Dissertation

Pekka Sjöman

Helsinki University of Technology
Faculty of Electronics, Communications and Automation
Department of Electronics

TKK Dissertations 153
Espoo 2009

VERY LOW NOISE CRYOGENIC RECEIVERS AND MEASUREMENT ELECTRONICS

Doctoral Dissertation

Pekka Sjöman

Dissertation for the degree of Doctor of Science in Technology to be presented with due permission of the Faculty of Electronics, Communications and Automation for public examination and debate in Auditorium S4 at Helsinki University of Technology (Espoo, Finland) on the 13th of February, 2009, at 12 noon.

Helsinki University of Technology
Faculty of Electronics, Communications and Automation
Department of Electronics

Teknillinen korkeakoulu
Elektroniikan, tietoliikenteen ja automaation tiedekunta
Elektroniikan laitos

Distribution:
Pekka Sjöman
DA-Design
Keskuskatu 29 B
31600 Jokioinen
FINLAND
URL: http://www.da-design.fi/
E-mail: pekka.sjoman@da-design.fi

ISBN 978-951-22-9747-4
ISBN 978-951-22-9748-1 (PDF)
ISSN 1795-2239
ISSN 1795-4584 (PDF)
URL: http://lib.tkk.fi/Diss/2009/isbn9789512297481/

TKK-DISS-2566

Multiprint Oy
Espoo 2009

ABSTRACT OF DOCTORAL DISSERTATION	HELSINKI UNIVERSITY OF TECHNOLOGY P.O. BOX 1000, FI-02015 TKK http://www.tkk.fi
Author Pekka Sjöman	
Name of the dissertation VERY LOW NOISE CRYOGENIC RECEIVERS AND MEASUREMENT ELECTRONICS	
Manuscript submitted 9.9.2008	Manuscript revised 11.12.2008
Date of the defence 13.2.2009	
☐ Monograph	☒ Article dissertation (summary + original articles)
Faculty Faculty of Electronics, Communications and Automation Department Department of Electronics Field of research Applied Electronics Opponent(s) D.Sc. (Tech.) Edgar Schmidhammer and D.Sc. (Tech.) Mikko Kuisma Supervisor Professor Pekka Eskelinen Instructor -	

Abstract

The purpose of this thesis was to develop very low noise cryogenic receivers and related high accuracy measurement setups to validate the operation of the receivers. Different types of cryogenic noise measurement setups were developed and compared. The noise measurement accuracy was improved for cryogenic temperatures at millimeter wave frequencies. A demonstrator was built for the continuous comparator receiver topology at millimeter waves. Measurement equipment were constructed to validate the receiver operation. Finally, an integrated 70 GHz continuous comparator receiver was built and suitable measurement tools were developed to ensure proper spacecraft operation.

Individual cryogenic amplifiers showed the best noise and gain results at the time of measurement. The noise temperature of the 20 K physical temperature split block mounted amplifiers was ~30 K, very close to its physical limits. The demonstrator receiver measurements expanded the knowledge of operation of continuous comparator millimeter wave receivers. A noise temperature of 40 K was measured for the demonstrator receiver, providing 1/*f*-knee frequencies lower than 10 mHz. The receiver topology was verified at 70 GHz with high stability at cryogenic temperatures. The integrated receiver was measured to have noise temperature of 30 K and a 1/*f*-knee frequency lower than 50 mHz. The integrated receiver was developed for the Elegant Bread Board (EBB) receiver in ESA's Planck Project. The required measurement equipment and facilities were built for spacecraft payload simulation. A large cryogenic chamber and cooling system were also designed and constructed for testing.

Keywords noise measurement, measurement electronics, cryogenic, millimeter wave, receiver	
ISBN (printed) 978-951-22-9747-4	ISSN (printed) 1795-2239
ISBN (pdf) 978-951-22-9748-1	ISSN (pdf) 1795-4584
Language English	Number of pages 141
Publisher Helsinki University of Technology, Faculty of Electronics, Communications and Automation	
Print distribution Helsinki University of Technology, Department of Electronics	
☒ The dissertation can be read at http://lib.tkk.fi/Diss/2009/isbn9789512297481/	

VÄITÖSKIRJAN TIIVISTELMÄ	TEKNILLINEN KORKEAKOULU PL 1000, 02015 TKK http://www.tkk.fi

Tekijä Pekka Sjöman

Väitöskirjan nimi
VERY LOW NOISE CRYOGENIC RECEIVERS AND MEASUREMENT ELECTRONICS

Käsikirjoituksen päivämäärä 9.9.2008	Korjatun käsikirjoituksen päivämäärä 11.12.2008

Väitöstilaisuuden ajankohta 13.2.2009

☐ Monografia	☒ Yhdistelmäväitöskirja (yhteenveto + erillisartikkelit)

Tiedekunta Elektroniikan, tietoliikenteen ja automaation tiedekunta
Laitos Elektroniikan laitos
Tutkimusala Sovellettu elektroniikka
Vastaväittäjä(t) TkT. Edgar Schmidhammer ja TkT. Mikko Kuisma
Työn valvoja Prof. Pekka Eskelinen
Työn ohjaaja -

Tiivistelmä

Työn aikana kehitettiin erittäin matalakohinainen kryogeeninen millimetriaaltoalueen radiovastaanotin ja mittausjärjestelmät toiminnan osoittamiseksi. Matalan lämpötilan kohinan mittausmenetelmiä pyrittiin parantamaan millimetriaaltoalueella. Kryogeeninen jatkuvasti vertailevan vastaanottimen demonstraatioversio ja mittausjärjestelmä rakennettiin. Lopuksi rakennettiin mahdollisesti avaruuteen lähetettävän vastaanottimen testaus- ja kelpoistamisjärjestelmä.

Työn aikana tehty demonstraatiovastaanotin perustui erittäin matalakohinaisiin vahvistimiin. Vahvistimien kohina ja vahvistus olivat mittaushetkellä tiettävästi paras mitattu tulos kryogeenisillä 70 GHz:n pakatuilla vahvistimilla. Demonstraatio-vastaanottimella tutkittiin jatkuvasti vertailevan vastaanottimen ominaisuuksia. Vastaanottimen 1/f-kohinan polvitaajuutta saatiin pienennettyä noin 4 kertaa pienemmäksi erillislaskennalla. Demonstraatiovaiheen jälkeen jatkuvasti vertailevan vastaanottimen etupää integroitiin yhdeksi kokonaisuudeksi, joka kylmennettiin 20 K lämpötilaan. Integroitu kokonaisuus oli tiettävästi ensimmäinen kryogeenisillä vaiheensiirtimillä toimiva V-alueen (70 GHz) jatkuvasti vertailevan vastaanottimen etupää. Myös vastaanottimen takapää (suodatin-vahvistin-ilmaisu-videovahvistin) integroitiin yhdeksi kokonaisuudeksi. Työssä tehtiin integroidun vastaanottimen mittaamiseen tarvittava laitteisto, jolla todennettiin vastaanottimen ominaisuudet ja sen avaruuskelpoisuus. Kryogeenisen matalakohinaisen vastaanottimen kohinan mittausjärjestelmän tarkkuutta parannettiin. Mittausjärjestelmässä voitiin mitata kohina kahdella eri tavalla ja samanaikaisesti oli mahdollista mitata vastaanottimen vaste.

Asiasanat vastaanotin, kohinan mittaaminen, kryogeeninen

ISBN (painettu) 978-951-22-9747-4	ISSN (painettu) 1795-2239
ISBN (pdf) 978-951-22-9748-1	ISSN (pdf) 1795-4584
Kieli Suomi	Sivumäärä 141

Julkaisija Teknillinen korkeakoulu, Elektroniikan, tietoliikenteen ja automaation tiedekunta

Painetun väitöskirjan jakelu Teknillinen korkeakoulu, Sovelletun elektroniikan laitos

☒ Luettavissa verkossa osoitteessa http://lib.tkk.fi/Diss/2009/isbn9789512297481/

Preface

The experimental part of this thesis work has been carried out at Ylinen Electronics Ltd., in close cooperation with MilliLab and with Metsähovi radio observatory during years 2000-2004.

I want to sincerely thank my supervisor, Professor Pekka Eskelinen, for his guidance and advice throughout this work. Frankly this work would never have been done without Professor Eskelinen's encouragement. I also wish to thank all my co-workers in Ylinen Electronics for their help and support.

The pre-examiners of this thesis, D.Sc. (Tech.) Edgar Schmidhammer and D.Sc. (Tech.) Jussi Säily, are gratefully acknowledged.

I would like to thank Lic.Sc. (Tech.) Petri Jukkala, B.Sc. (Tech.) Nicholas Hughes and D.Sc. (Tech.) Pekka Kangaslahti at Ylinen Electronics for giving me the opportunity to make this work during the Planck project and for their valuable advice.

Professor Jussi Tuovinen at VTT MilliLab is warmly acknowledged for his enthusiasm for the receiver technology and the Planck project. Without Professor Tuovinen the 70 GHz Planck project would have been done in some other country in Europe.

I would like to thank to my friends and colleagues M.Sc. (Tech.) Sami Ovaska and M.Sc. (Tech.) Mikko Laaninen. Mikko and Sami used nervebreaking months, even years, to study the receiver behaviour.

I want to thank my parents, who have have been encouraging and supportive throughout my studies. I want to thank my sister, Pauliina, for reminding me of life outside engineering science. My warmest gratitude is addressed to my family; my wife, Elina, for her support and, our daughters, Ilona and Iiris, for giving sunshine almost every day.

Jokioinen, 3rd of January, 2009

Pekka Sjöman

Contents

List of publications

The experimental part of this thesis is described in the following scientific publications, referred to in the text by the abbreviations P1-P7. The papers are sorted to assists the reader to follow the work done, not just according to their scientific appreciation.

P1 P. Sjöman, T. Ruokokoski, P. Eskelinen, "Noise measurements of individually packaged 70 GHz radio astronomical amplifiers for the Planck satellite mission", *Proceedings of the URSI GA 2002*, Maastricht, the Netherlands, 2002

P2 P. Sjöman, P. Jukkala, N. Fabritius, P. Eskelinen, S. Urpo, "43 GHz cryogenic LNAs for radio astronomic VLBI-receiver", *Helsinki University of Technology, Radio Laboratory Publications*, Report S 257, URSI/IEEE XXVII Convention on Radio Science, Espoo, 2002

P3 S. Ovaska, P. Sjöman, P. Eskelinen, "Theoretical susceptibility of Planck 70 GHz radiometer to systematic effects", *Metsähovi Publications on Radio Science, HUT-MET-48*, 15 p., 2003

P4 P. Sjöman, P. Eskelinen, T. Ruokokoski, "1/f-noise studies of 70 GHz continuous correlation receiver", *European Frequency and Time Forum*, St. Petersburg, Mar.12-14, 2002

P5 P. Sjöman, N. Hughes, P. Jukkala, S. Ovaska, J. Tuovinen, P. Kangaslahti, P. Eskelinen, "A cryogenic microwave measuring system for satellite receiver testing", *Proceedings of the European Microwave Conference*, vol. 33, pp. 81-83, 2003

P6 P. Sjöman, T. Ruokokoski, N. Hughes, P. Jukkala, P. Kangaslahti, S. Ovaska, P. Eskelinen, "Planck satellite 70 GHz EBB-version back-end module", *IEEE Aerospace and Electronic Systems Magazine*, vol. 18, No. 5, pp. 22-25, 2003

P7 P. Sjöman, N. Hughes, P. Jukkala, S. Ovaska, J. Varis, J. Tuovinen, "An ultra low noise cryogenic 70 GHz wide band continuous comparator receiver" *Proceedings of the 3rd ESA Workshop on Millimetre Wave Technology and Applications*, Espoo, pp. 75-80, 2003

The author's contribution in [P1 – P7] has been as follows:

In Paper [P1], the present author was the main contributor. The LNA design was made by Pekka Kangaslahti, D.Sc.. Petri Jukkala, Lic.Sc, supervised the research work and Professor Pekka Eskelinen assisted in writing the manuscript.

In Paper [P2], the present author was the main contributor. Professor Pekka Eskelinen assisted in writing the manuscript.

Paper [P3] is the result of collaborative work between Sami Ovaska, M.Sc., and the present author. The calculations and measurements were conducted together with Sami Ovaska at Ylinen Electronics, and the manuscript was also written in cooperation with Sami Ovaska.

In Paper [P4], the present author was the principle contributor. The facilities, measurement software, measurements and the assembling of the demonstrator receiver were carried out by the author. The work was supervised by Petri Jukkala, Nicholas Hughes and Professor Jussi Tuovinen. Professor Pekka Eskelinen assisted in writing the manuscript.

In Paper [P5], the author was the primary contributor. The cryogenic chamber and measurement facilities were designed by the author. Nicholas Hughes supervised the electronic interfaces of the receiver. Professor Jussi Tuovinen and Petri Jukkala supervised the measurements. Professor Pekka Eskelinen assisted in writing the manuscript

Paper [P6] is a collaborative work. The mechanical design of the back-end was a cooperative effort between Teemu Ruokokoski and the author. The radiotechnical design was made by the author and the remaining design by Petri Jukkala and Nicholas Hughes. Professor Pekka Eskelinen assisted in writing the manuscript.

Paper [P7] is the result of collaborative work. The design of the front-end was made by Nicholas Hughes. The back-end receiver design was made in cooperation with Teemu Ruokokoski. The verification measurement equipment and the measurements were made by the author. The design and the measurements were supervised by Professor Jussi Tuovinen and Petri Jukkala. Professor Pekka Eskelinen assisted in writing the manuscript.

Abbreviations

ACA	Amplifier Chain Assembly
BEM	Back-end Module
CMB	Cosmic Microwave Background
CMTS	Cryogenic Microwave Test System
COBE	Cosmic Background Explorer
CW	Continuous Wave
DA	Digital to Analog
DUT	Device Under Test
DVM	Digital Voltage Meter
EBB	Elegant Breadboard
EM	Engineering Model
EMC	EletroMagnetic Compatibility
ENR	Excess Noise Ratio
ESA	European Space Agency
FEM	Front-end Module
FFT	Fast Fourier Transform
FM	Flight Model
GPS	Gigahertz-Peaked Spectrum
HEMT	High Electron Mobility Transistor
HFI	High Frequency Instrument
IF	Intermediate Frequency
InP	Indium Phosphide
LFI	Low Frequency Instrument
LNA	Low Noise Amplifier
LO	Local Oscillator
NASA	National Aeronautics and Space Administration
NTP	Normal temperature and pressure
MAP	Microwave Anisotropy Probe
MMIC	Monolithic Microwave Integrated Circuit
OMT	Orthomode Transducer
PC	Personal Computer
PSD	Power Spectral Density
PWM	Pulse-Width Modulation
QM	Qualification Model
RF	Radio Frequency
RSS	Root Sum of Squares
RT	Room Temperature
SPC	Science Programme Committee
SSB	Single Side Band
TRL	Through-Reflection-Load
TVA	Temperature Variable Attenuator
TVL	Temperature Variable Load
VLBI	Very Long BaseLine
VNA	Vector Network Analyser
VTT	Technical Research Centre of Finland

Symbols

a	Device factor of the detectors
a	Waveguide dimension
A	Amplifier stability constant
b	Waveguide dimension
B	Bandwidth
C	Device dependent gain fluctuation constant
f	Frequency
f_c	Center frequency
f_k	Knee frequency
G	Amplifier gain
g_m	Transconductance of individual HEMT
$g(t)$	Time dependent amplifier voltage gain
I	Current
I_d	Drain current
k	Boltzmann's constant
l	Length of waveguide
L_{in}	Attenuation of input waveguide
L_{out}	Attenuation of output waveguide
L_{TVA}	Attenuation of TVA
L_{WG}	Waveguide loss
Lz	Loss in z-dimension
N_s	Number of stages of LNA
N_d	Number of detector diodes
$n(t)$	Time dependent amplifier noise temperature
P_{in}	Input power
P_{tot}	Total AC power of detector
r	DC gain ratio
R	Reference signal
R_s	Surface resistance
S	Sky signal
S_{11}	Scattering parameter from port 1 to port 1

S_{12}	Scattering parameter from port 2 to port 1
S_{21}	Scattering parameter from port 1 to port 2
S_{22}	Scattering parameter from port 2 to port 2
T_{BE}	Test receiver noise temperature
T_C	Cold noise temperature
T_{DUT}	Noise temperature of DUT
T_H	Hot noise temperature
T_{in}	Physical temperature of input waveguide
$T_l(z)$	Temperature of losses in z-dimension
T_{ni}	Noise temperature of LNAs
T_{NS}	Noise temperature of noise source
T_{sys}	System Noise Temperature
T_{TVA}	Physical temperature of TVA
T_{wg}	Waveguide temperature
T_x	Noise temperature
T'_x	Noise temperature reduced to DUT input
T_y	Noise temperature of reference signal
Y	Y-factor
V_d	Drain voltage
$V_d(t)$	Detected voltage
$\overline{V_d}$	Time average of detected voltage
$\overline{V_{DC}}$	Time average of DC voltage
V_e	BEM power supply voltage
V_g	Gate voltage
$\overline{V_{out}}$	Time average of output voltage
$x(t)$	Sky noise voltage
$y(t)$	Reference load noise voltage

α	Spectral index
δ	Relative deviation of amplifier noise temperatures
ΔL_{in}	Uncertainty of L_{in}
ΔL_{TVA}	Uncertainty of L_{TVA}
ΔT	Radiometer sensitivity

ΔT_{DUT} Uncertainty of T_{DUT}

ΔT_{equiv} Mimicked input signal

$\Delta T(f)$ Spectral density of ΔT

ΔT_{in} Uncertainty of T_{in}

ΔT_{TVA} Uncertainty of T_{TVA}

ΔV Voltage sensitivity

ΔY Uncertainty of Y-factor

ε Relative deviation of amplifier gains

ε_r Permittivity

η Free-space wave impedance

κ Waveguide roughness coefficient

K Comparison coefficient

λ Wavelength

λ_0 Free-space wavelength

μ_0 Permeability of vacuum

ρ_m Resistivity of waveguide material

τ Post integration time

φ Deviation of phase shifts

1 Introduction

1.1 General

Every time we look at the sky with a radio telescope, in a sense we travel back in time. That measurable energy is the farthest and the most ancient and can be thought of as the remains of a shock wave from the Big Bang, occurring about 13730 million years ago. Today, this energy is called the Cosmic Microwave Background (CMB). Thus, when measuring CMB, we are also looking back in time, observing this primeval energy is like seeing the Universe as it was almost at its origin. Satellite radio receivers have been developed to measure this energy accurately enough to predict the first microseconds at the start of the Universe. The advantage of satellite receivers over ground-based telescopes is that they are undisturbed by the Earth's atmosphere.

Planck (formerly known as COBRAS/SAMBA) was selected in November 1996 by ESA's Science Programme Committee (SPC) to become the 3rd medium-sized mission (M3) in the Agency's Horizon 2000 programme of scientific missions. The Science Management Plan of Planck (ESA/SPC(97)27) was approved by SPC in June 1997 [1].

The Planck mission was designed to image the anisotropy (often referred to as fluctuation) of the CMB over the whole sky. NASA's satellite COBE (Cosmic Background Explorer) was the first to detect the anisotropy in 1992. Following this discovery, several experiments conducted from the Earth were able to confirm the results. Before COBE, astronomers had unsuccessfully searched for anisotropies. The apparent uniformity of the CMB in these experiments was due to a lack of sensitivity and resolution [2]. Subsequently, NASA launched a second CMB satellite: MAP (Microwave Anisotropy Probe). The measurement accuracy of MAP compared to COBE was like comparing a microscope to an eye.

The Planck satellite will map the structure of the CMB in unprecedented detail, providing more accurate measurements than those offered by previous missions, due to its higher angular resolution, better sensitivity and broader frequency coverage. Compared to MAP, the Planck satellite is about 2-3 times more sensitive. The Planck

spacecraft carries two instruments: the Low-Frequency Instrument (LFI) and High-Frequency Instrument (HFI), covering the frequencies from 30 GHz to 77 GHz and 100 GHz to 857 GHz, respectively (Table 1.1). The satellite structure is shown in Figure 1.1 a) and the LFI mock-up with horn antennas in Figure 1.1 b). In the original design definitions, the LFI also had a 100 GHz channel, enabling cross-calibration between LFI and HFI. Unfortunately, due to the lack of available funding, the 100 GHz LFI receivers were canceled.

Table 1.1. Planck satellite original receivers.

Insrument	LFI				HFI					
Center Frequency (GHz)	30	44	70	100	100	143	217	353	545	857
Detector Technology	HEMT LNAs				Bolometers					
Detector Temperature	20K				4K					
Number of detectors	4	6	12	34	4	12	12	6	8	6
Bandwidth %	20	20	20	20	25	25	25	25	25	25
Angular Resolution (arcmin)	33	23	14	10	10	8	5.5	5	5	5
Average $\Delta T/T \cdot 10^{-6}$, 1s	1.6	2.4	3.6	4.3	1.7	2.0	4.3	14.4	147	6670

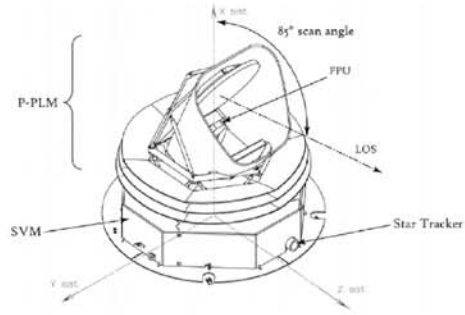

a)

b)

Figure 1.1. a) a Planck satellite, and b) a plastic 1:1 mockup of the LFI receivers connected to the satellite chassis.

The LFI will produce full-sky maps at 30, 44 and 70 GHz, with an angular resolution of 33', 23'and 14', respectively, and with an average sensitivity per resolution element

$\Delta T/T \approx (2\text{-}4)\cdot 10^{-6}$. By comparison, the COBE provided a sensitivity of $\Delta T/T \approx 10^{-5}$, and an angular resolution of 7 degrees at 53 GHz [2]. The unprecedented angular resolution and sensitivity values will uncover a wealth of cosmological information encoded in the anisotropy pattern at degree and sub-degree angular scales [3]. This will answer a number of truly fundamental questions about our Universe: How fast is the Universe expanding? What is the ultimate fate of the Universe? What are its material constituents (baryons, dark matter, etc.)? Where did the initial perturbations come from? When did the first structures form in the Universe?

The LFI measurements will determine the primary cosmological parameters (Hubble constant, deceleration parameter, curvature of space, baryon density, dark matter densities, including neutrinos, amplitude and the spectral index of primordial scalar density perturbations, and the gravity wave content of the Universe) to an accuracy of a few percent [2,4]. In the LFI frequency range, the contaminating effect of the galactic emission, dominating the astrophysical foreground noise on a scale lower than 30', has its minimum at around 60 GHz, while confusion noise due to extragalactic sources, dominating on smaller angular scales, has a minimum at a range of 100-200 GHz, primarily due to radio sources. The 70 GHz channel is therefore optimal for achieving the cleanest possible view of primordial CMB fluctuations over the full range of angular scales. The astrophysical foreground noise is expected to be well below the cosmological signal for all observed angular scales.

To meet scientific requirements, it was necessary to develop the state-of-the-art receiver. The available MMIC noise temperatures were about twice as high as the required 25 K. In addition, operation of some of the key components (LNAs and phase switches) was unknown at cryogenic temperatures. The requirements and complexity of the receiver, not to mention the testing and qualification of the receiver, made the schedule very tight. A rough schedule of the Planck Project is shown in Figure 1.2.

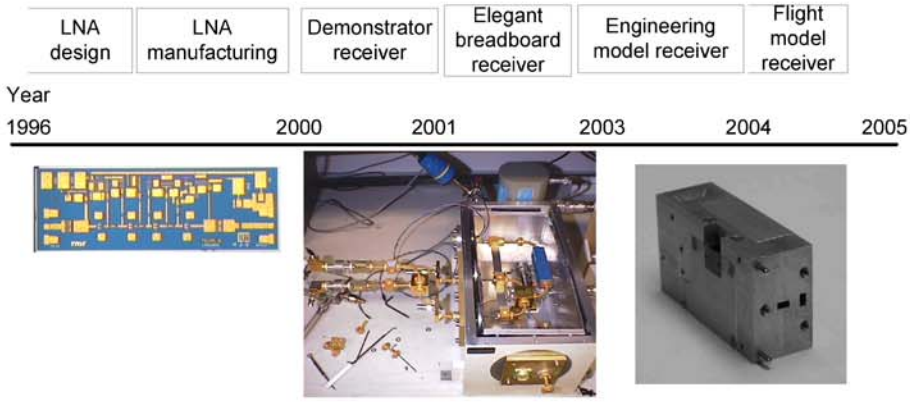

Figure 1.2. Rough schedule of the Planck Project.

The Finnish LFI team formed by MilliLab, Metsähovi Radio Observatory and YLINEN Electronics Ltd. significantly contributed to both the design and manufacture of the cryogenic very low noise continuous comparator receiver at 70 GHz. MilliLab originally initiated the Finnish involvement and became supplier of the 70 GHz receivers. YLINEN Electronics Ltd. and Metsähovi were subcontractors in the manufacturing, design and testing of all the critical parts of the 70 GHz receiver.

1.2 Scope and contents of this thesis

Much development work was done focusing on state-of-the-art MMIC LNAs and phase switches. That work, however, did not form part of this thesis and was carried out by other Planck team members. Individual components were first measured at cryogenic temperatures to verify their operation and performance. The demonstrator receiver was then built to study the effect of the phase switch modulations, feasible gain and phase match of parallel amplifiers, as well as the stability of the receiver. After building the demonstrator, the next step was to integrate the receiver in order to meet the mass and volume requirements. More than one year of work was devoted to testing the Elegant Bread Board receiver (EBB). For test purposes, a special Cryogenic Microwave Test System (CMTS) was built.

Chapter 2 outlines the theoretical background of the continuous comparator receivers. Chapter 3 introduces several new amplifier and receiver designs. Chapter 4 describes

the “foxtrot” phase switching method with cryogenic LNAs in the demonstrator receiver. Chapter 4 also presents a complete test setup for the EBB receiver and the receiver tests.

1.3 New scientific and technological achievements

The work presented in this thesis contains the following main findings and new results.

1. The feasibility of cryogenic millimeterwave LNAs has been demonstrated. The LNAs achieved the lowest known noise temperature in the world, as measured at cryogenic temperatures within the operational frequency band.
2. Several cryogenic noise temperature measurement techniques were studied at millimetre waves. Improved TVAs were developed for noise measurement.
3. An improved 1/*f*-noise cancellation method was presented for the continuous comparator receiver.
4. A cryogenic V-band continuous comparator receiver was built with integrated phase switches for the first time.
5. The lowest noise and 1/*f*-noise results have been obtained for a V-band continuous comparator receiver.

2 Theoretical aspects of the receivers

The 70 GHz Planck radiometer is a wide-band pseudo-correlation receiver based on four-stage 0.1 µm gate length Indium Phosphide (InP) High Electron Mobility Transistor (HEMT) Monolithic Microwave Integrated Circuit (MMIC) amplifiers processed by NGST [5]. The phase shifters are based on InP diodes and also processed by an NGST InP process. The total radiometer consists of a corrugated horn antenna, an Orthogonal Mode Transducer (OMT), a 20 K Front-End Module (FEM) and a 316 K Back-End Module (BEM), as shown in Figure 2.1. The horn antenna and OMT are supplied by a collaboration between LABEN and Custom Microwave. The other parts of the 70 GHz receivers are supplied by collaboration between MilliLab, Ylinen Electronics Ltd. and the Metsähovi Radio Observatory [6].

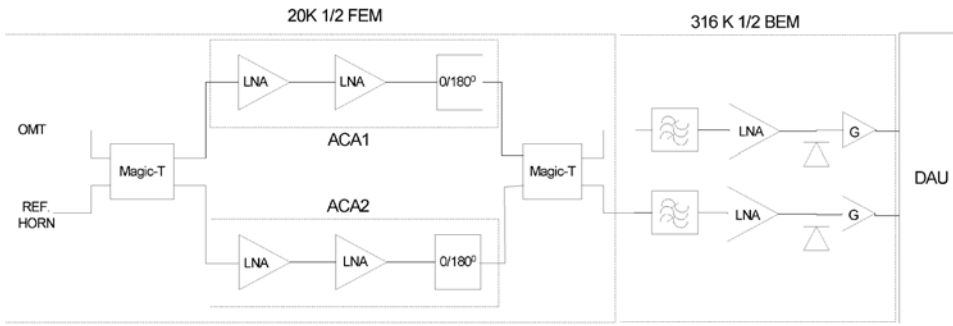

Figure 2.1. A block diagram of half of the receiver, i.e., the receiver for one polarization.

The signal of the other parallel Amplifier Chain Assemblies (ACA) is continuously phase shifted by a $0/180^{o}$ switch. The parallel phase switch is mounted for amplitude and phase similarity. The output signal of the detector diode is then a continuous stream of sequential sky and reference signals. The comparison between the parallel detector diode signals could have been done by using both of the phase switches; however, to simplify the Data Acquisition Unit (DAU), the switching is performed with only one phase shifter.

In the Planck LFI, the final sampling time is 122 μs at the level of the data acquisition board. The sampling frequency is then reduced on board by averaging consecutive sky and reference load samples in order to arrive at a final sampling frequency that corresponds to one sample for every third of a beam width. This implies that the final sampling frequency is of an order of 33 Hz for the 30 GHz channel and 77 Hz for the 70 GHz channel. The Planck satellite scans the sky in almost great circles at 1 rpm (16 mHz). To avoid 1/*f*-noise contamination of the CMB maps, the 1/*f*-noise knee frequency should be smaller that the spin frequency, although some of the 1/*f*-noise can be removed from the final CMB maps [7-9]. The receiver has to perform a continuous comparison to remove the fluctuation of the RF amplifiers and DC electronics during the long integration time [10-15]. The balanced FEM amplifiers suppress the effect of gain fluctuations on the front-end LNAs if the gain, phase and noise are matched well enough between parallel amplifier chains [8,16]. The back-end generated 1/*f* fluctuation is suppressed by switching the phase switches faster than 1/*f*-knee frequency of the components. The phase switching frequency (4096 Hz) is selected to be higher than the normal 0.1 μm gate length InP-HEMT amplifier knee frequency (500Hz) [10].

A detailed analysis of the Planck satellite continuous comparator receivers can be found in [8] and [16]. A brief summary is shown below and can be found in [P3]. For the continuous comparator receiver, the ideal sensitivity is

$$\Delta T = \frac{2T_{sys}}{\sqrt{B\tau N_d}}. \tag{2.1}$$

Where T_{sys} is the receiver system noise temperature, B is the effective bandwidth, τ is the integration time and N_d is the number of diode outputs. N_d is 2 if both hybrid outputs are detected, monitored and averaged properly. The detected and post-calculated output voltage of the diode at the phase state i is

$$V_{di}(t) = \frac{a}{2}\left[\left(\frac{x(t)+y(t)}{\sqrt{2}}+n_1(t)\right)g_1(t)+\left(\frac{x(t)-y(t)}{\sqrt{2}}+n_2(t)\right)g_2(t)\right]^2$$
$$-r\frac{a}{2}\left[\left(\frac{x(t)+y(t)}{\sqrt{2}}+n_1(t)\right)g_1(t)-\left(\frac{x(t)-y(t)}{\sqrt{2}}+n_2(t)\right)g_2(t)\right]^2, \tag{2.2}$$

where $V_{di} = V_{d1} - rV_{d2}$, $x(t)$, $y(t)$ are the sky and reference input voltage vectors, and $n_i(t)$ and $g_i(t)$ are i'th ACA's noise voltage and voltage gain vectors, respectively. The detector conversion factor is a, and r is a DC-gain ratio to null the output voltage after detection. The gain fluctuation has been studied in several publications [14-17]. The r-value can be selected to minimize the effect of amplifier noise or gain fluctuations [12],[13]. The multiplication with the r-value is normally done in post-detection to provide more system flexibility. If the different voltage signals are not correlated, cross correlation terms, such as $\overline{n_1 n_2}$, will vanish. Then, the output voltage becomes

$$\overline{V_d} = \frac{akB}{4}(1-r)\left(G_1(T_x + T_y + 2T_{n1}) + G_2(T_x + T_y + 2T_{n2})\right)$$
$$+ \frac{akB}{2}(1+r)\sqrt{G_1 G_2}\,(T_x - T_y), \qquad (2.3)$$

where k is Boltzmann's constant ($1.38 \cdot 10^{-23}$ J/K), and B is the effective bandwidth. T_x and T_y are the sky and reference inputs temperatures, respectively. In the ideal case, gains in the ACA 1 and 2 are identical $G_1 = G_2 = G$ and also the noise temperatures $T_{n1} = T_{n2} = T_n$. Then, the r-value can be selected to be

$$r = \frac{T_x + T_n}{T_y + T_n} \qquad (2.4)$$

to null the output and minimize the $1/f$ fluctuation . The receiver output $\overline{V}_{out}$ is

$$\overline{V}_{out} = \frac{\overline{V}_{d1} + \overline{V}_{d2}}{2}. \qquad (2.5)$$

For the relative sensitivity spectrum ($\Delta T/T$) with small input temperature differences, the following assumption can be made

$$\frac{\Delta T}{T} = \frac{\Delta V}{V} = \frac{\overline{V}_{out}}{\overline{V}_{DC}}, \qquad (2.6)$$

where $\overline{V}_{DC}$ is

$$\overline{V}_{DC} = \frac{\overline{V}_{DC1} + \overline{V}_{DC2}}{2}. \tag{2.7}$$

$\overline{V}_{DC1}$ and $\overline{V}_{DC2}$ are diode 1 and 2 detected voltages. The relative gain fluctuation can be modeled as

$$\frac{\Delta G(f)}{G} = \frac{C}{f^{\alpha}}, \tag{2.8}$$

where C is a device dependent constant. For a four stage cryogenic 0.1 µm InP HEMT, C is estimated to be $1 \cdot 10^{-4}$, and α is a low frequency spectrum shape constant, normally in the range 0.45-0.5 [17-23]. If the LNA is properly designed, the noise temperature fluctuations are related to g_m fluctuation, given as

$$\frac{\Delta T_{ni}(f)}{T_{ni}} \cong \frac{1}{2\sqrt{N_s}} \frac{C}{\sqrt{f}} = \frac{A}{\sqrt{f}}. \tag{2.9}$$

The A parameter for V-band cryogenic amplifiers is about $2.5 \cdot 10^{-5}$ [8]. Therefore, the ideally balanced radiometer sensitivity in the presence of 1/*f*-noise can be approximated, see also [P3], as

$$\Delta T = T_{sys} \sqrt{\frac{2}{B\tau} + \frac{C^2}{f}}. \tag{2.10}$$

3 Equipment design and construction

The equipment constructed in this thesis consists of millimeter wave radio components and test setups to validate their operation. The designed components are for radio astronomical use, and the component design specifications were written based on the assumption of the best possible operation. The main criteria for radio astronomical receivers are minimum noise temperature, stability, minimum 1/*f*-noise and maximum (at the given bandwidth) effective bandwidth. The test setups were designed specifically for this research based on the spacecraft requirements.

3.1 Low noise split block amplifiers

Two different packaged cryogenic amplifiers were designed for radio astronomical use. One for a ground-based telescope at the Metsähovi radio observatory, and the other for the Planck demonstrator receiver. The telescope amplifiers were for the 43 GHz VLBI receiver.

3.1.1 43 GHz VLBI receiver amplifiers

The 43 GHz amplifiers were needed for the 43 GHz receiver (see also [P2]) to measure GPS sources over a long time period for predicting the burst amplitudes for the Planck satellite CMB map algorithms. The 43 GHz receiver will also be used for VLBI measurements. The amplifier specifications stem from VLBI requirements [24]:

-<50K noise temperature @ 20K

->40 dB gain @ 43GHz

-Operational frequency band 42 – 44 GHz

-High stability

-Physical dimensions to match the 43 GHz receiver design

The selection of possible MMIC amplifiers was based on the specifications as well as earlier experience with the selected chips. The selected InP-MMIC-HEMTs were from HRL 0.1 μm InP-process [25]. The MMIC design was completed for the 60 GHz Planck receiver, as the frequency was at the early stage of the project. However, because of

good low frequency behavior, the same chip could be used at 43 GHz. There were 3- and 4-stage MMIC designs of the InP-HEMTs. The four-stage design was selected for the 43 GHz amplifier because it had better stability and higher gain. Because of a high gain requirement, two four-stage MMICs were mounted in series and the first chip could be optimized for minimum noise operation while the second chip was biased to give maximum gain.

The WR-22 waveguide to 0.1mm alumina microstrip transition was based on a K-connector center pea. A circular beryllium copper stub was soldered to one end of the K-pea to improve the match from the waveguide to the K-pea. A picture of the LNA is shown in Figure 3.1.

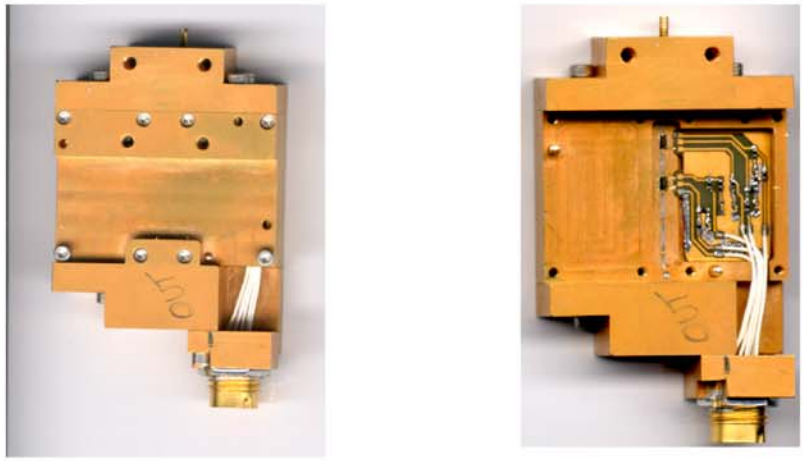

a) b)

Figure 3.1. a) the LNA with and b) without lid.

The amplifier contains a resistive voltage divider 1:10 for the gate voltages and 10 nF capacitors for gate and drain voltages. The first chip was biased with two different gate voltages and one drain voltage, while the second chip had only one voltage for gate and drain, as shown in Figure 3.2.

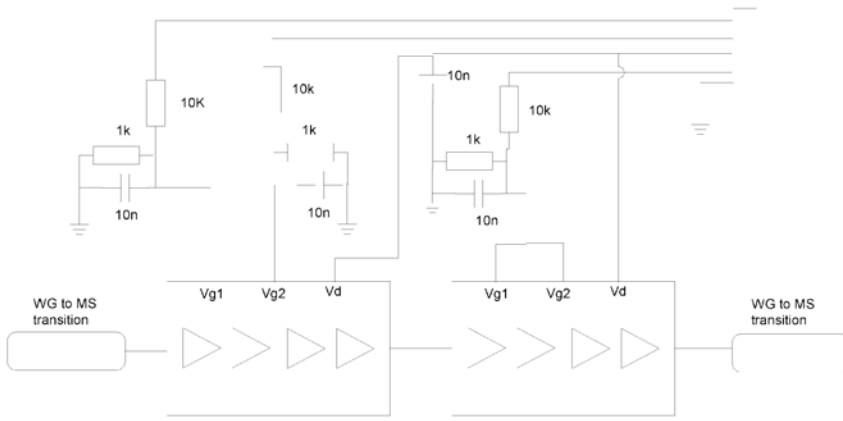

Figure 3.2. A schematic of the 43 GHz amplifiers.

3.2 70 GHz split block amplifiers

Very low noise amplifiers and their noise behaviour have been studied widely over the past decade. [25-41] InP-based processes have demonstrated the best noise performance at cryogenic temperatures. For the Planck 70 GHz receiver, the amplifier chips were prosessed in an NGST 0.1 um InP-HEMT process. The design of the MMIC chips is described in [5, 6], but remains beyond the scope of this thesis. This thesis focuses on the amplifier integration, verification and measurement test setups.

The amplifier split block package was designed to minimize the input losses before amplifier chips. Therefore, the input transition from the waveguide to the microstrip was designed for minimum length, as well as to provide as good match as possible [42]. To minimize the waveguide losses, the division plane of the split block was in the maximum E-field plane of the TE_{10} mode in the waveguide. Figure 3.3 shows the split block design. The package is made of gold plated brass.

a) b)

Figure 3.3. a) an individual split block amplifier, b) the MMIC and transitions inside the split block.

The gate voltages have 50 Ω series resistors and 10 nF shunt capacitor. The drain voltage has only a 10 nF shunt capacitor with a possible series resistor to stabilize the amplifier, as shown in Figure 3.4.

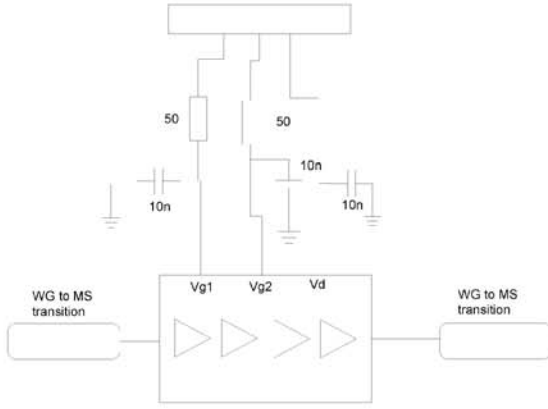

Figure 3.4. A schematic of the 70 GHz LNA.

3.3 Planck demonstration receiver

The demonstration system was designed to be flexible and reliable, as well as to approximate the final flight topology as closely as possible. The demonstration receiver was built to prove the continuous comparator receiver operation as well as to study the different phase switching schemes. For flexibility reasons, only the first LNAs were in the cryochamber and the external electronics was designed to be capable of using different phase swiching schemes. The block diagram of the demonstration receiver is

shown in Figure 3.5. The demonstrator was made with separate split block components, thus enabling every component to be measured individually.

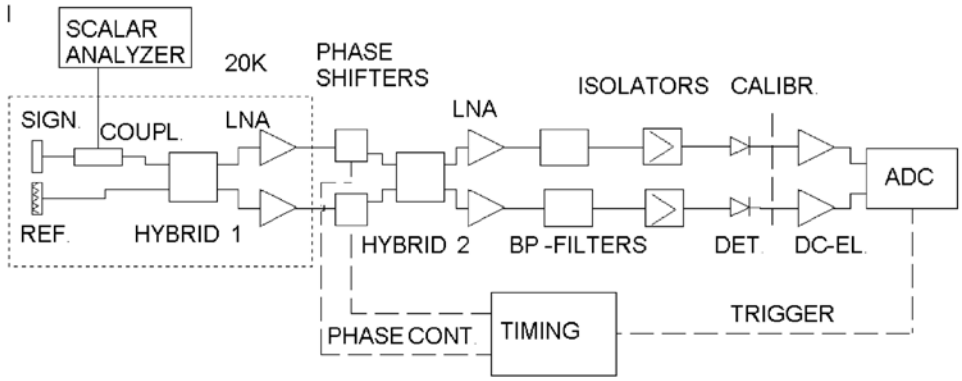

Figure 3.5. A block diagram of the 70 GHz Planck satellite demonstration receiver and the associated 1/f-noise test system.

The signal and reference loads in Figure 3.5 represent the sky and reference signals of the receiver. Both are implemented with a matched waveguide load having a return loss lower than –35 dB over the entire WR-15 waveguide frequency range. The loads consisted of Eccosorb® MF117 absorber pyramids in the waveguide with internal heater resistors. The manufactured multihole directional coupler was designed to have 20 dB coupling and lower than 0.4 dB insertion loss. The hybrids were Millitech CMT-12-R60S0 magic-Ts. The LNAs were NGST InP-MMIC-HEMTs, as described in section 3.2. Phase shifters were Pacific mm-Product 6090m. The detectors are ELVA ZBD-15 zero-biased diode detectors. Figure 3.6 shows the layout of the demonstrator receiver in the cryostat.

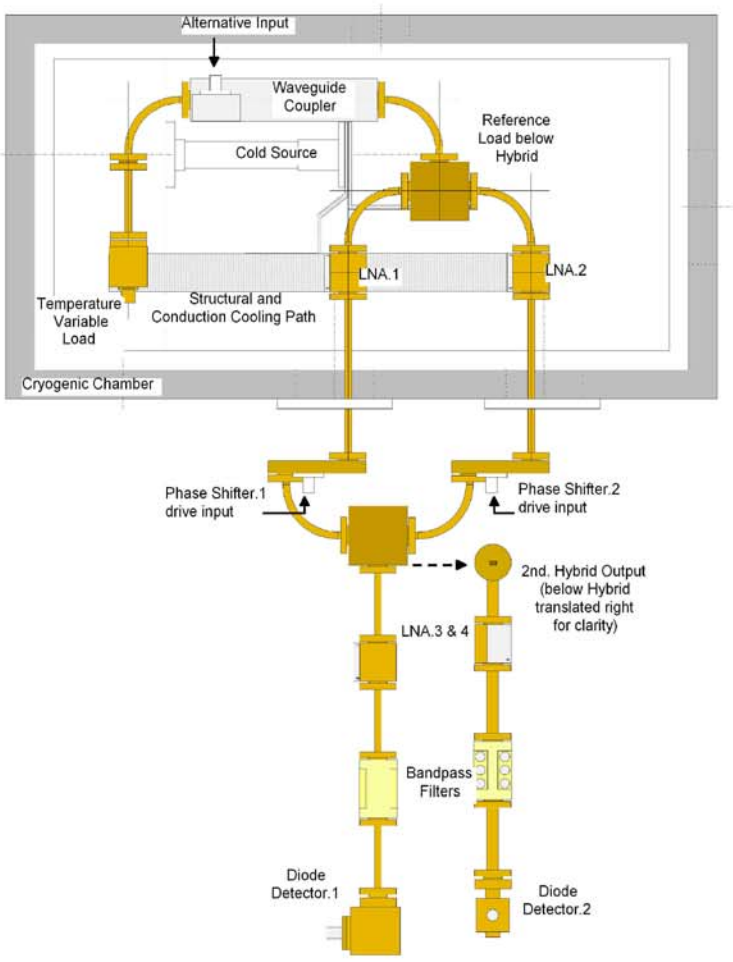

Figure 3.6. The layout of the demonstrator receiver in the cryostat.

The DC module, including DC amplifiers, integrators and sample&hold circuits, was specifically constructed as a separate printed circuit board for these measurements. The ADC card used was a Microstar DAP4000a/112. Dedicated external timing electronics were designed to give control voltages to the phase shifters, a trigger signal to the ADC card and integrate/reset and sample/hold commands to the external electronics.

3.4 The Elegant Breadboard (EBB) Front-end Module (FEM)

After completing the demonstrator measurements, the next phase was to integrate the receiver Front-end module (FEM) as one block. The designed FEM should meet the

satellite payload volume (45.1mm x 28.7mm x 30mm) and mass requirements (150g) as well as meet the radio technical operation requirements [43]. It was decided that the FEM design would be as symmetric as possible in order to ease the phase match between parallel chains. The block diagram of the EBB FEM is shown in Figure 3.7.

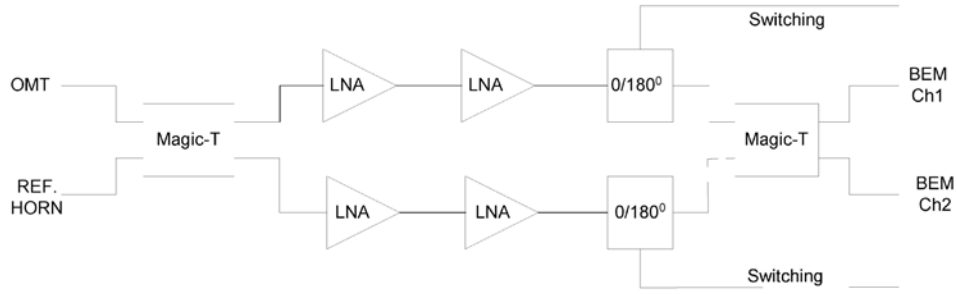

Figure 3.7. The block diagram of one half of the EBB FEM.

The losses before LNAs must be kept as low as possible because of the required noise temperature. For that reason, it was decided that the hybrids would be waveguide magic-T. The magic-Ts were simulated individually to minimize simulation time. The performance was optimized to the operational frequencies [44]. The magic-Ts must have 20dB isolation between isolated channels, about 10 degrees phase match between channels and the lowest possible insertion loss at the operating frequency band. The design was also verified as having highest-grade manufacturing tolerances to improve the yield. The magic-Ts were also built and tested as individual components providing close to simulated results, at room temperature, (Figure 3.8).

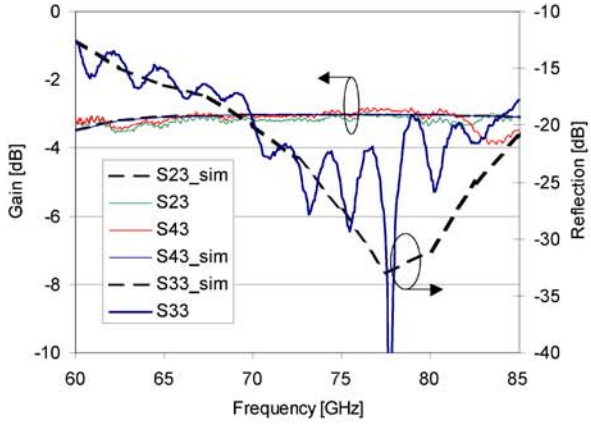

Figure 3.8. Simulated and measured magic-T insertion losses and reflection from the sky port to ACA ports (Δ - 2 and 4).

The waveguide to microstrip transmission lines was also simulated and measured individually. The design was based on [42]. Transmission lines were mounted in a WR-12 package for cryogenic testing, showing good performance (Figure 3.9). The WR-12 package used was actually physically similar to ACAs. Hence, the magic-T and straight feed-troughs can be tested together to determine whether there would have been standing waves at the input (Figure 3.10).

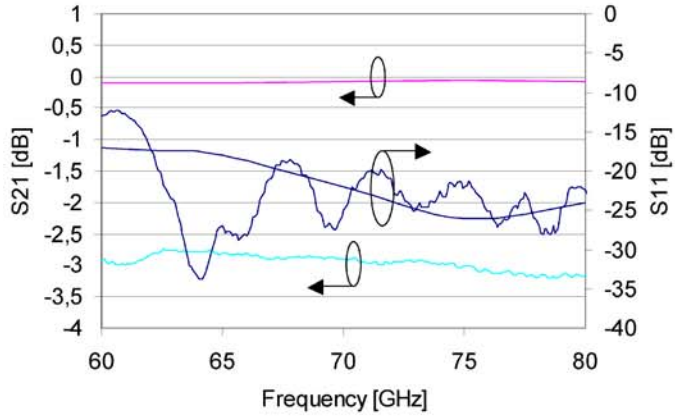

Figure 3.9. Waveguide to microstrip transmission simulation and measurement results at room temperature. The measurement contains 20 mm long 50 Ω line on 0.1 mm alumina substrate made from 2 mm long pieces. The thick lines denote measured values and the thin lines represent simulated values. If the 20 mm long 50Ω lines on 0.1mm thick Alumina substrates are eliminated from the results, the transmission insertion losses are of the order of 0.1 dB.

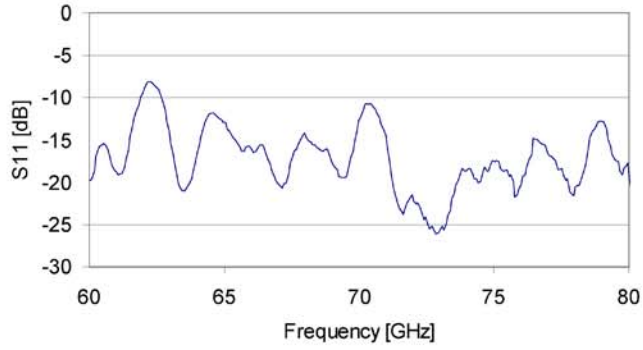

Figure 3.10. FEM input match with microstrip through ACAs at room temperature.

The FEM halves were identical and connected to the OMT outputs. The reference horn, the λ/4 chokes around it, and the magic-Ts were milled to the FEM bodies. The ACAs were mechanically identical and also electrically as close as possible to each other. The mechanical model of the ACA and one half of the receiver are shown in Figure 3.11.

The ACAs can be measured separately, with the best pairs being selected on the basis of gain and noise match.

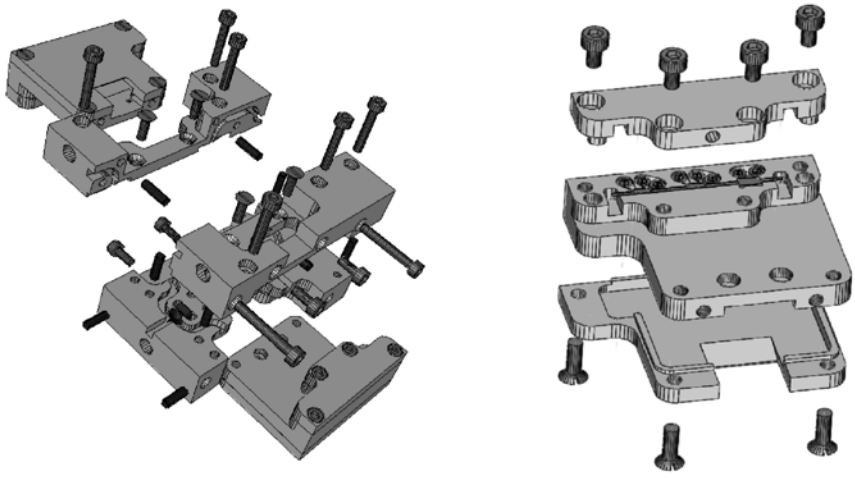

a) b)

Figure 3.11. The mechanical model of Planck FEM; a) structural view of the FEM body and ACAs and b) structural view of one ACA.

The ACAs have a bias protection circuit at the bottom side and feed-throughs are used to route the bias voltages to the MMICs (Figure 3.12). The physical size of one half of the FEM is 45.1mm x 28.7mm x 15mm. Both the FEM and the ACAs are composed of nickel-gold plated aluminium. The allowed power dissipation for the full FEM is 20.8 mW and for the full BEM 604 mW.

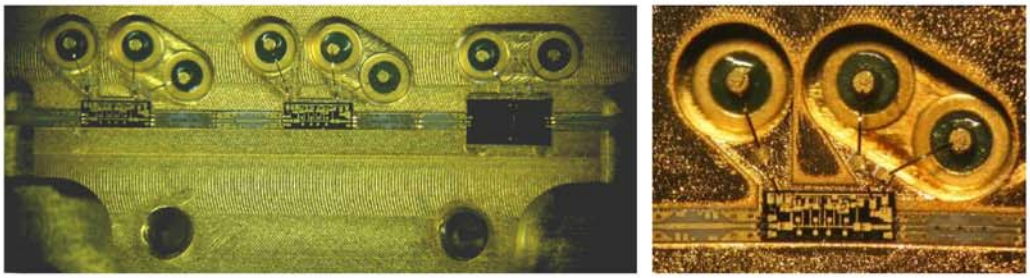

a) b)

Figure 3.12. a) ACA RF-chain, b) the second LNA of the ACA and the bonded feed-trough. From the right: microstrip-coplanar transition from the first LNA, the MMIC chip and 3 dB attenuator before phase shifter to improve the LNA-phase shifter match.

3.5 Back-end Module (BEM) of the receiver

The measured microwave background radiation is about 3 K at 70 GHz. The antenna noise temperature is 30 K and FEM has a gain of 45 dB. The input power of the BEM is 190 nW with an effective bandwidth of 14 GHz. The operating band is limited in the BEM with band pass filters and the RF signal is amplified to be in the square law region of the diode detector. A BEM block diagram is shown in Figure 3.13.

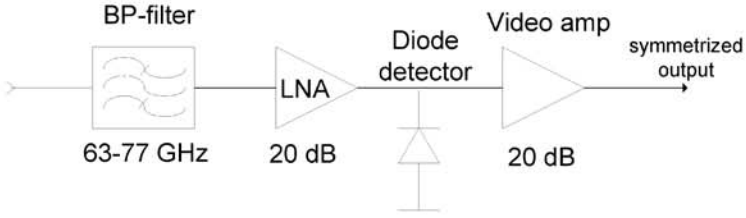

Figure 3.13. A functional block diagram of the 70 GHz Planck satellite back-end module.

The H-plane WR-12 waveguide filter is the first operational block of the BEM to minimize unwanted waveguide to microstrip transitions, and because of the wide passband, there was no risk of LNA instability. The final filter was designed with an HFSS® electromagnetic field simulator [45]. Five- and six-cavity Chebyshev flattop

passband filters were selected. The simulated and measured waveguide filter frequency responses are shown in Figure 3.14.

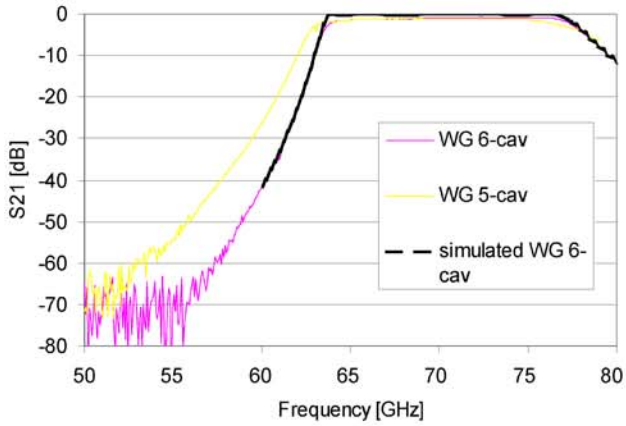

Figure 3.14. Measured S_{21} of five- and six-cavity and simulated S_{21} of 6-cavity H-plane WR-12 waveguide filter.

As shown in Figure 3.14, the measured five-cavity filter is shifted to lower frequencies and the losses are similar in both filters. The six-cavity filter was selected for the BEM. The LNAs were measured individually on-wafer, and the bias points were optimized for optimum gain for each amplifier. The selection of the BEM LNAs was based on as flat gain as possible over the receiver operating frequency band. A typical frequency response and noise figure of the LNAs at room temperature are shown in Figure 3.15.

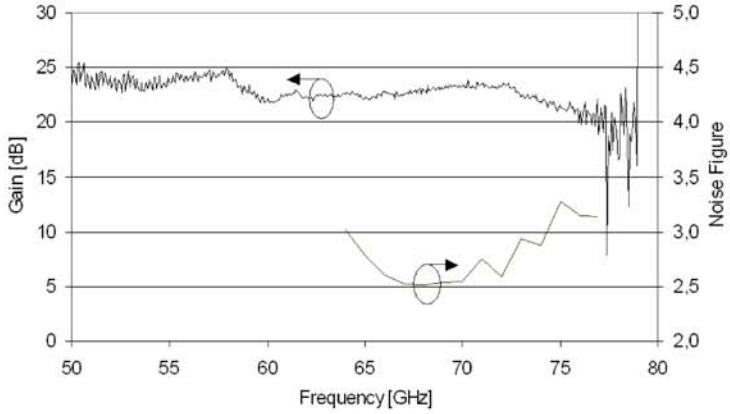

Figure 3.15. An individual split block packaged LNA's gain and noise figure. The upper-band ripple is due to the measurement setup.

The diode detector design was based on Agilent Technologies zero-biased HSCH-9161 Schottky detector diodes. The design was chosen to be a one diode solution for the sake of simplicity, although two-diode structures might have been more sensitive [46]. Moreover, the 1/*f*-noise behaviour of the detector diode is not critical for the continuous comparator design. The design was implemented with an ADS® simulator. The chosen detector substrate was 0.1 mm alumina with the same height as the 3 dB matching attenuator before the detector diode. High ε_r was selected to minimize the needed size of the layout. The diode detector PCB was made using a thin-film process at Ylinen Electronics.

Diode detectors were measured individually in the split block packages. The total power radiometer has to be in the linear region of the diode detector [47]. In Figure 3.16, the diode sensitivity curves are shown with different load resistors.

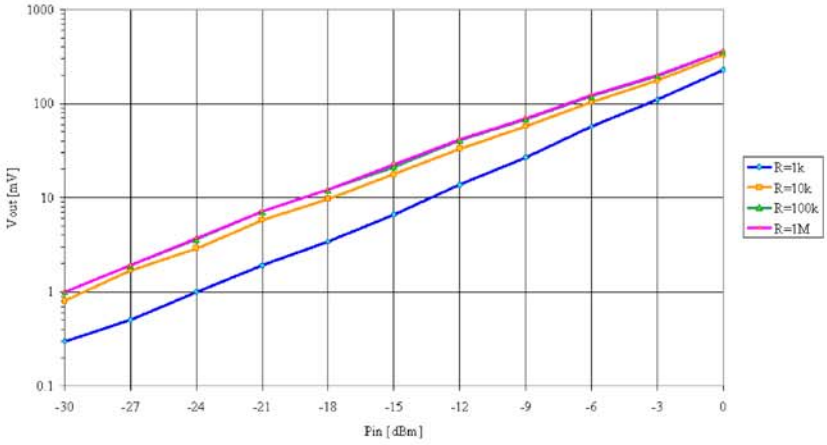

Figure 3.16 Diode detector sensitivity with 70 GHz CW signal and different load resistors.

For the final design, R3 and R4 were selected as the 50 kΩ load resistors (Figure 3.17). OP27 operational amplifiers were selected for the video amplifiers. This selection was made from the ESA preferred parts list. The OP27 is not the best operational amplifier from the perspective of stability and noise behaviour [48]. It has a noise specification of $3\text{nV}/\sqrt{\text{Hz}}$. The schematic of the video amplifiers is shown in Figure 3.17. The video amplifier design was implemented with the minimum number of components to minimize the PCB area and the cost of the BEM.

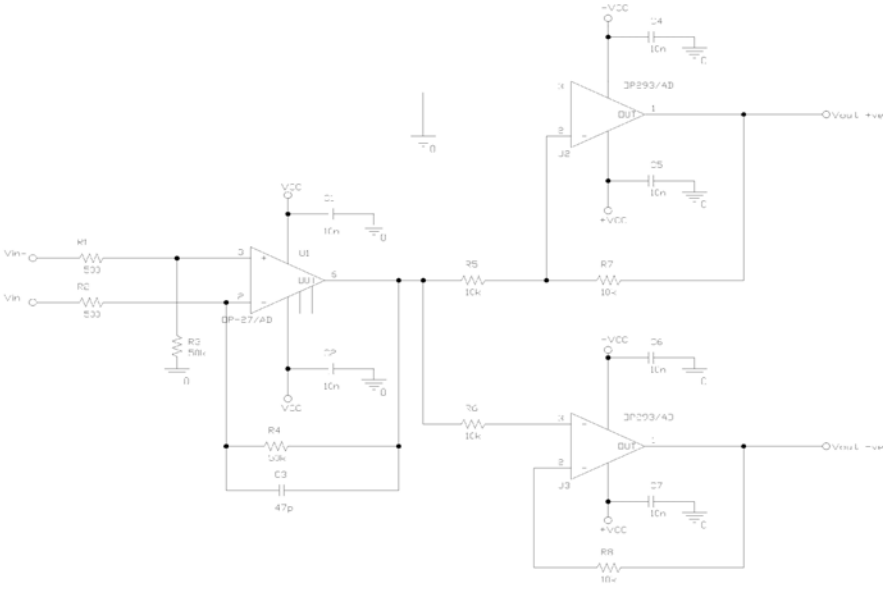

Figure 3.17. EBB BEM video amplifiers.

The mechanical design of the BEM was implemented with a Mechanical desktop 5. The envelope for the BEM was 15x30x90 mm^3. All four channels with filter, LNA, detector, video amplifiers, bias supplies and connectors had to fit inside the given envelope. The final EBB BEM mechanical structure is shown in Figure 3.18.

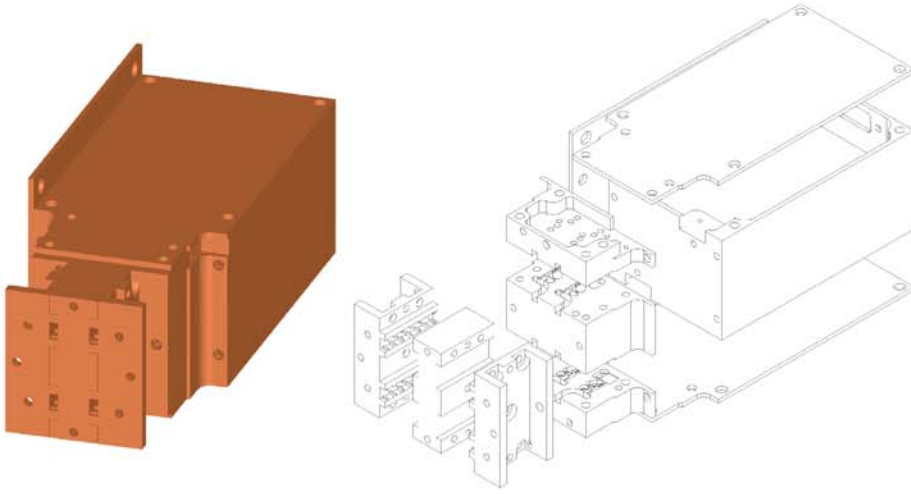

Figure 3.18. The final EBB BEM structure. The major dimensions are 70x40x40 mm^3.

The design allowed the waveguide filters, LNA-detector modules and video amplifiers to be separated and measured individually. The RF parts were made symmetric in order to find the best match between filters and LNAs when differences were noted between chains.

4 Test setups and measurements

The developed test setup consists of three different cryogenic test systems: One for the ACA amplifiers, a second test system for the demonstrator, and a third system for the complete receiver testing. The demonstrator test system was also used for individual amplifier testing with some modifications. The tests normally consist of noise, gain, isolation, match, power consumption, EMC and 1/*f*-noise measurements. These all were measured at room (300 K) and cryogenic (20 K) temperatures. In addition, the operation of the DUT had to be optimized to meet the in-flight requirements, Table 4.6.

4.1 Test setup and measurements of individual amplifiers

The individual amplifiers and demonstrator receiver were tested in the same cryogenic chamber. Only the waveguides inside the chamber needed to be changed from the individual amplifiers tests to demonstrator tests. The cryogenic system consists of a vacuum pump, aluminium vacuum chamber and the CTI-Cryogenics 220 helium cooler. The WR-15 waveguide feed-throughs to the vacuum were made with two 5 µm thick mylar sheets at the waveguide flange interfaces. The reason for the WR-15 feed-throughs (not WR-12) was that the Planck receiver was required to have a center frequency of 60 GHz and was thus built with a WR-15 waveguide [49]. The center frequency change from 60 GHz to 70 GHz occurred during assembly of the demonstrator, though most of the components were already bought for the WR-15, resulting in the use of the original chamber design. All the measurements and optimizations were done at an operational bandwidth of 63–77 GHz.

The noise measurement setup was designed to meet the need for fast tuning of the amplifiers as well as to be as reliable as possible. At the same time, the gain of the DUT had to be measured with high accuracy. The noise measurement setup for the individual amplifiers is shown in Figure 4.1.

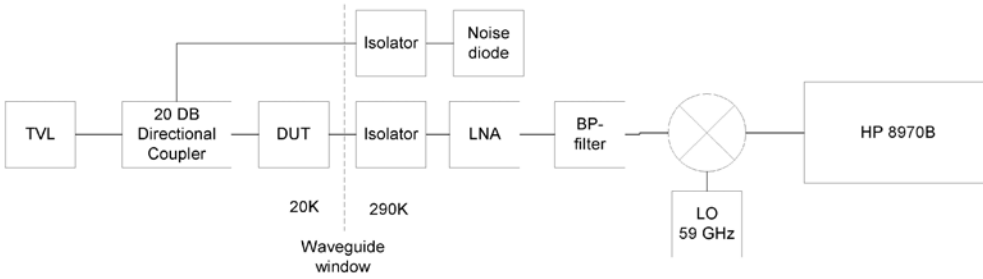

Figure 4.1. A block diagram of the individual LNA noise measurement test system.

The noise measurement setup was based on the HP 8970B noise test system. An HP 83557A mm-signal source module was used to generate the LO frequency to the external mixer. A 20 dB LNA was used as a preamplifier before the mixer to increase the input power to the mixer and HP8970B as well as to maximize the measurement accuracy. A Millitech WR-15 biased mixer was used as the external mixer. A PC was used to control the temperatures of the DUT and the temperature variable waveguide load (TVL) as well as to record data from the HP8970B and to control the LO source.

Waveguide parts inside the cryogenic chamber were measured with a VNA at room temperature. Coupling and insertion loss of the selected directional coupler and the return loss of the TVL are shown in Figures 4.2 a) and b), respectively.

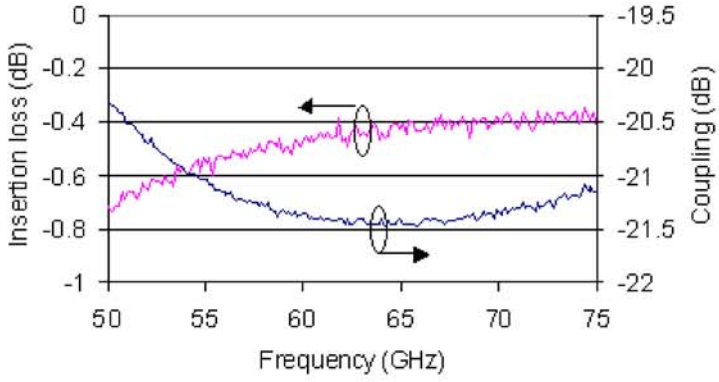

a)

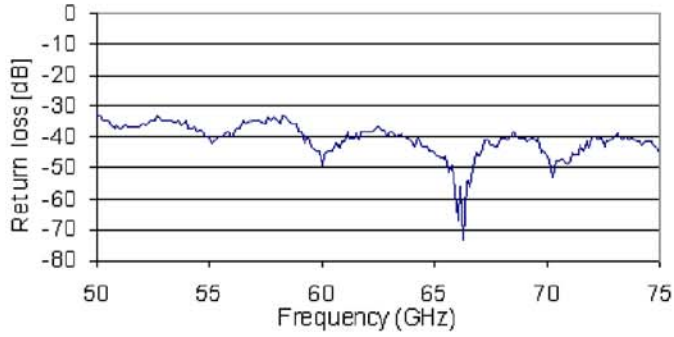

b)

Figure 4.2. a) 20 dB coupler coupling and insertion loss, b) TVL return loss at room temperature.

The coupling of the coupler was selected to be ~20 dB in order to obtain an adequate noise temperature from the noise diode used as well as to minimize the room temperature leakage through the coupler. The temperature variable load consisted of an Eccosorb MF-117 absorber pyramid inside a copper waveguide. The cryogenic gain calibration was performed with a 10 mm long copper waveguide in the place of the DUT. Input losses were estimated with cryogenic S_{11} measurement from the chamber input to the input of the direction coupler. Output losses were also measured from the output of the chamber to the output of the DUT. Coupling of the coupler at cryogenic temperatures was estimated from the loss measurements and gain measurements.

For individual amplifier measurements, two LNAs from the NGST Cryo4-wafer were mounted into a WR-15 split block structure (Figure 3.3). The noise was tuned to the optimum at bias points (V_d=0.5 V, I_d=15 mA, V_{g1}=270 mV, V_{g2}=265 mV) per one MMIC. The noise temperatures were measured at 20 K with the Temperature Variable Load (TVL) heated to a hot temperature of 60 K. The noise results were compared with externally calibrated noise diode measurements. Separate measurements agreed to within ±5 K. The gains were measured with VNA. The bias voltages V_d, V_{g1}, V_{g2} were tuned about ±30% from the optimum noise bias points separately. Gain and noise values were measured at every bias point. The gain and noise sensitivities to bias voltages were calculated and polynomial fits were made for every bias voltage value. The gain and noise temperature sensitivities for the bias voltages are shown in Figure 4.3. The amplifier gain and noise characteristics could have simply been modeled as a function of drain current, but the Planck satellite on-board electronics monitors the gate and drain voltages. The measured polynomial fit can be used for the satellite onboard device tuning if the LNA bias point or temperature changes during the flight.

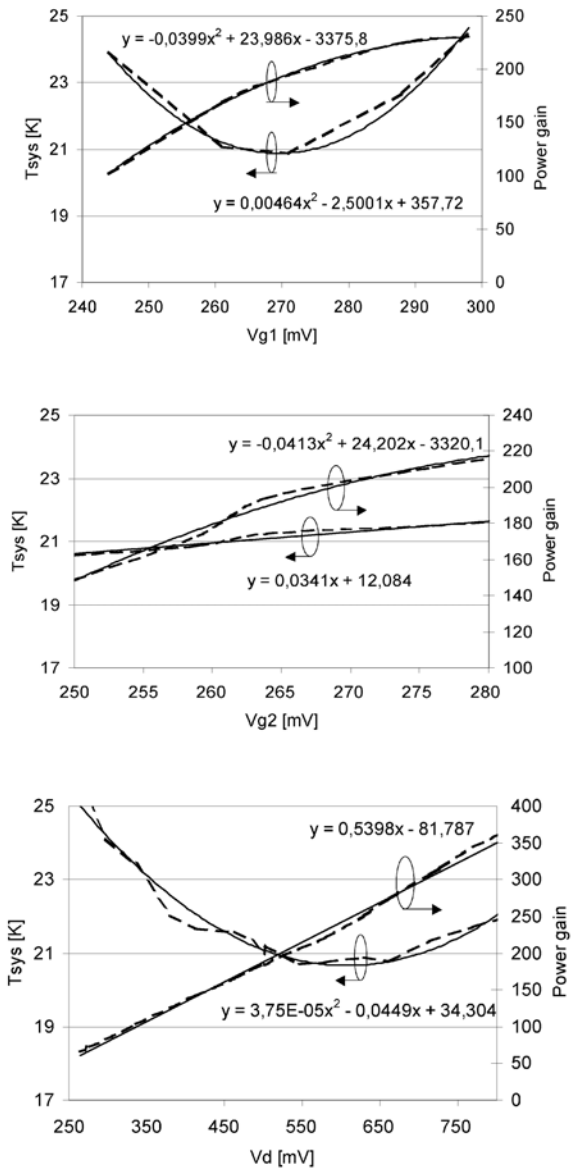

Figure 4.3. LNA gain and noise behavior as a function of bias voltages at a physical temperature of 20 K.

As shown in Figure 4.3, the drain and gate1 (which is connected only to the first transistor gate) voltages change the gain and noise dramatically, while gate 2 (connected to the three other gates) has only a minor effect on the noise temperature. Power dissipation was also calculated from the measured voltages and currents. The results indicate that the drain voltage mainly affects the gain and power dissipation of the amplifiers; gate 1 voltage mostly affects the noise temperature; and gate 2 voltage has only a minor effect on the noise temperature and gain. Gate 1 variations are shown in greater detail in Figure 4.4.

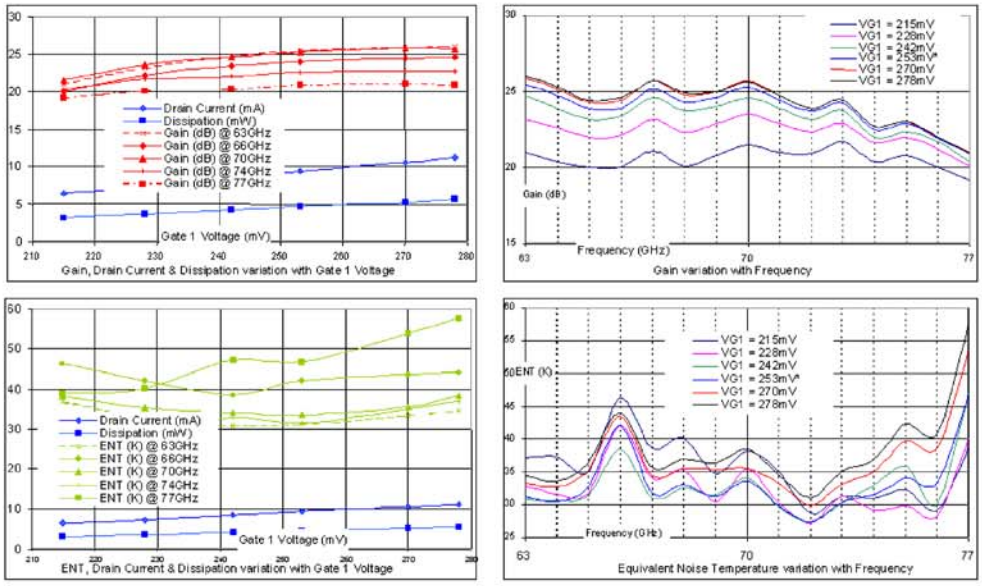

Figure 4.4. Cryogenic LNA results at 20 K with V_{g1} variation.

4.1.1 43 GHz LNA measurements

The 43 GHz LNA cryogenic measurement setup was built into the same dewar as the 70 GHz setup. The 43 GHz LNA noise temperature was measured in the cryogenic chamber with a temperature variable load (TVL). In paper [P2], the temperature variable load actually refers to the temperature variable 30 dB attenuator. An external scalar network analyzer HP 8757A was used to measure the gain of the LNAs. A measurement test setup is shown in Figure 4.5.

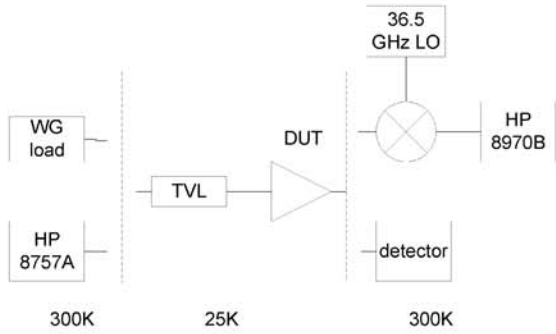

Figure 4.5. The test setup for the 43 GHz noise and gain measurements.

The gain of the LNAs was optimized with the scalar analyzer (Figure 4.6).

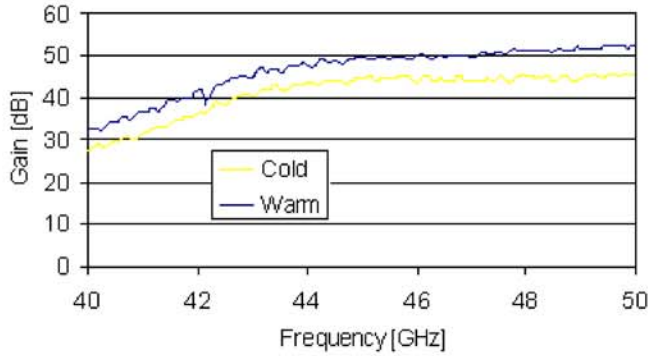

Figure 4.6. LNA3 gains at 295 K and 25 K.

The slope at the lower frequency end is a feature of the MMIC chips used. The difference between warm and cold gains is due to the different bias points. The cold temperature bias point (V_d=0.5V, I_d=23 mA) was optimized for minimum noise, while the warm bias point (V_d = 0.7 V, I_d =30 mA) was optimized for maximum gain. The attenuator was heated up to 53 K to obtain an adequate 1.8 dB Y-factor over the entire measured frequency band. The noise response of a cooled LNA3 is shown in Figure 4.7.

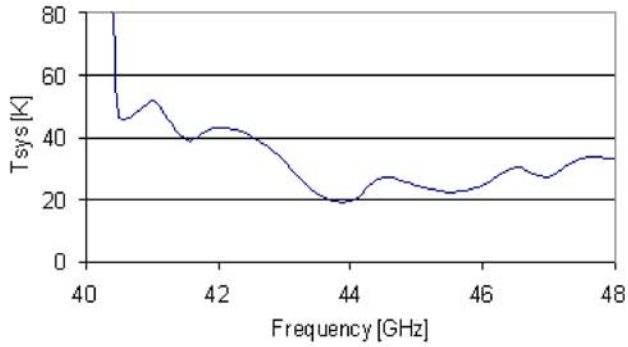

Figure 4.7. LNA3 noise temperature at a physical temperature of 25 K.

The noise response shows a noise temperature of less than 30 K between 43-47 GHz. At the lower frequency band, the chip is not in the optimum noise region because of poor input match.

4.2 Test setup and measurements of the demonstrator receiver

The demonstrator receiver block diagram was shown in Figure 3.3 in Section 3.3. The overall physical layout of the test arrangement with the demonstration receiver mounted in the cryostat is illustrated in Figure 4.8.

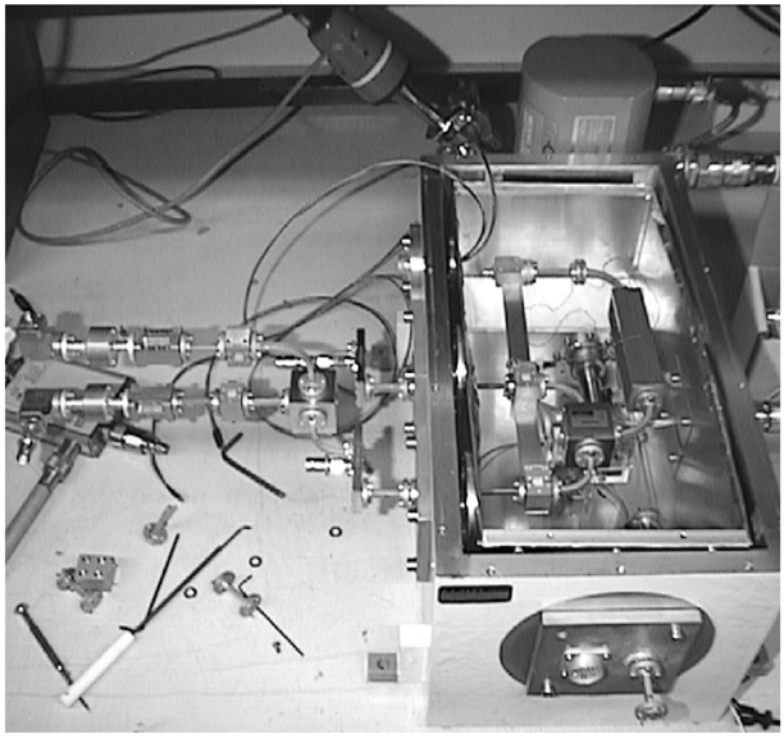

Figure 4.8. Demonstration receiver mounted in the cryostat. From the left: outside the dewar are detectors, isolators, waveguide filters, back-end LNAs, magic-T, phase shifters. Inside the dewar are LNAs, magic-T coupler and TVLs.

The cryogenic LNAs of the receiver were measured individually to optimize their bias points for noise, gain and power dissipation. The demonstrator amplifier chains were tuned to a gain balance with scalar analyzer measurements and by simultaneously tuning their bias voltages. These bias points were selected as close as possible to the optimum combination of gain, noise and power dissipation of individual amplifiers in terms of repeatability and measuring uncertainty. The phase switches were tuned to give a similar treatment, in which the bias voltage did not affect the switching operation. The electrical lengths of the amplifier chains were also matched with waveguide shims to reach the best isolation over the entire operating frequency band (Figure 4.9).

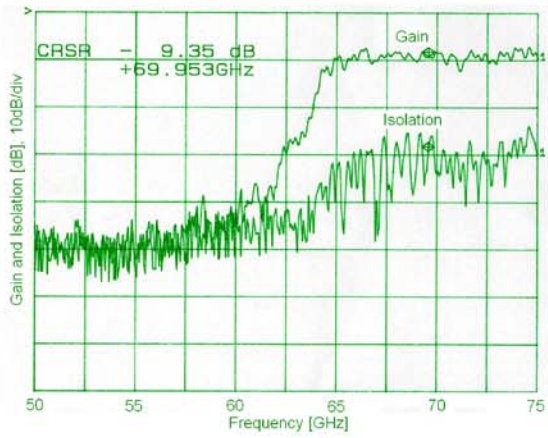

Figure 4.9. Gain (uppet curve) and isolation (lower curve) from chamber input to back-end filter output, scale 10 dB/div. The back-end filter limits the operation bandwidth to 63-77 GHz.

The total gain could be calculated from the loss measurements, where the input directional coupler was measured using 10 mm long copper waveguides in the place of DUT. Input and output waveguide losses were also measured with the reflection method. All the measurements were repeated at room temperature and 20 K. The input losses were also used for noise measurement corrections.

The system noise temperature of the receiver was next measured with a commercial noise measurement system (HP 8970B). Different input noise temperatures for a reasonable Y-factor were attained by heating the matched loads with heater resistors as well as by using a calibrated noise diode. The receiver noise temperature was optimized with LNA bias voltages using the noise diode. Typical noise behavior is shown in Figure 4.10.

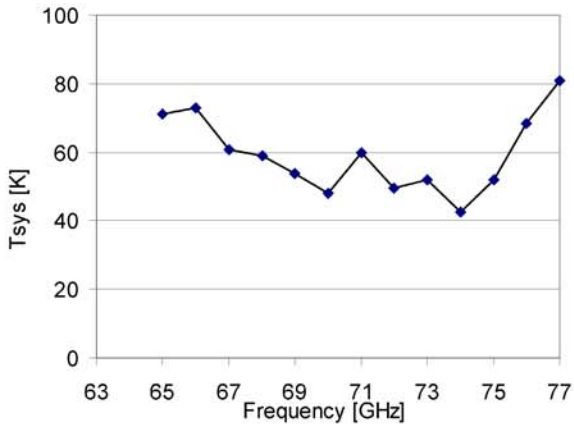

Figure 4.10. Typical noise response of the Planck demonstrator receiver at 20 K.

For the $1/f$ tests, the test system calibration was performed with a 50 Ω load directly connected to the AD-converter inputs of the external electronics. Naturally, the same trigger frequency was used as during the final receiver measurements with a data acquisition rate of 1 kHz. About 2 million points were recorded for later analysis. During the analysis, the noise spectrum was created according to the Welch method using a 1000-point overlap between data from different FFTs for the r-value calculation [50]. A post integration time of 0.5 s was used to create a more accurate low-frequency region of the spectrum. Boxcar windowing was used in the calculations [50]. The calculation was made as similar as possible to that during known satellite operation. The channel 1 "signal" and "difference" are shown in Figure 4.11.

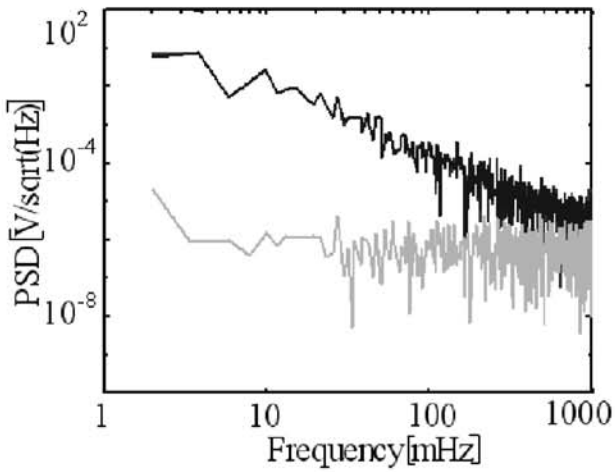

Figure 4.11. The measured 1/f spectrum of the test system with a 0.5s post integration time. The black line represents the measured signal and the grey, lower line shows the calculated difference between the signal and reference.

The knee frequencies of the signal and the reference are both at about 4 Hz, but the knee frequency of their difference is less than 4 mHz. Similar results were observed with an open load and detector diode connected to the system input from both AD channels.

The 1/*f*-noise was measured as a function of signal and reference temperatures and at different phase switching speeds. In all measurements, the phase switchs were used as "foxtrot" (Table 4.1)

Table 4.1. Phase switch positions in a single "foxtrot" cycle.

Cycle	1	2	3	4
Ph. Sw. 1	0	180°	0	180°
Ph. Sw. 2	0	0	180°	180°

The basic idea in this phase switching scheme is the enhanced cancellation of 1/*f*-noise in the test system. Because the signal and reference both pass through the two parallel amplifier chains, back-ends and DC amplifiers, the system 1/*f*-noise can be minimized

in a post-detection calculation. The data was synchronously recorded from both diode detectors.

The "reference" signal was warmed to four different temperatures from 20 K to 36 K with a resistor and a linear laboratory power supply because the external temperature PWM control system (Lake Shore 330) generates about 1 Hz of noise to the calculated spectrums. This gave the differences as -0.6 K, 1.5 K, 5.5 K and 14.5 K, respectively. LNA temperatures were also recorded, and the change from 19 K to 23 K was observed while heating. Both measured diode detector voltages gave similar results. The diode voltage is proportional to the sum of one input noise temperature and the average noise temperature of the amplifiers. In order to computationally null the system 1/*f*-noise, the result from one of the states has to be multiplied by a constant *r*, which was calculated from the end of the measured spectrums just at the point when white noise first appears, as was shown in Chapter 2. The measured knee frequency as a function of respective r-values shows a parabolic nature, as indicated in Figure 4.12. The knee frequency was obtained visually from the spectrums, leading to some error in the shape of the curve. The calculated optimum r-value of the test data was 1.0816. Power spectrums of the measured data at different reference load temperatures and optimum r-values are shown in Figure 4.13.

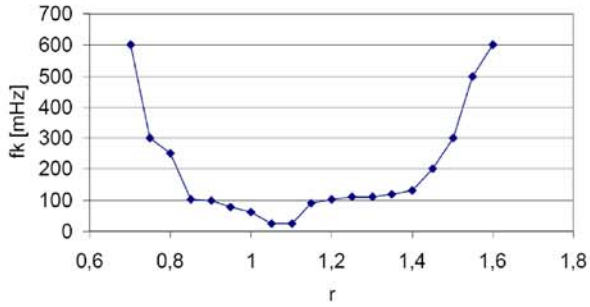

Figure 4.12. Behavior of the knee frequency f_K versus different r-value. A temperature difference of –0.6 K was observed between the signal and reference. The calculated optimum r-value was 1.0816.

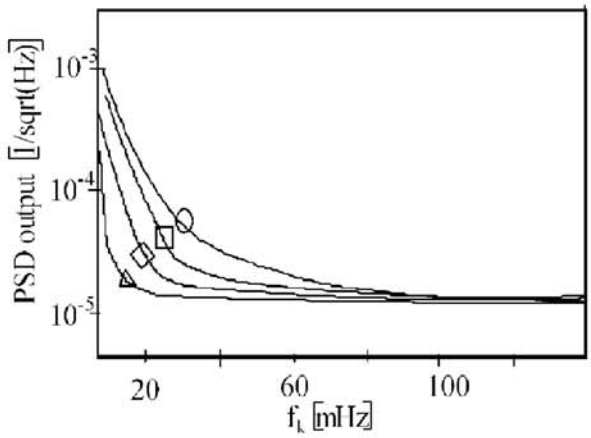

Figure 4.13. Smoothed 1/f power spectrums at various temperature differences between signal and reference loads. An optimum r-value for each case was used. The triangle indicates –0.6K, diamond 1.5 K, square 5.45 K and circle 14.49 K difference between signal and reference loads. Note: the scale is $1/\sqrt{Hz}$*, i.e., the PSD spectrum value was divided by the measured diode voltage. The ideal white noise level (ΔV/V) with one phase shifter is* $2.4 \cdot 10^{-5}$ $1/\sqrt{Hz}$ *with 0.5 s post integration time and an effective frequency bandwidth of 14 GHz.*

The reference load temperature was increased and both "foxtrot" (with two modulating phase shifters) and single phase shifter modulation measurements were performed using the same sampling rate for all tests. An increase was observed in the PSD 1/*f*-knee frequency near 200 mHz. This is due to the averaged *r*-value, which does not totally cancel out all of the back-end electronics drifts, and 1/*f*-noise of back-end LNAs. Dedicated r-values minimize that effect. An averaged r-value is calculated as

$$V_{out} = S(1) + S(2) + S(3) + S(4) - r(R(1) + R(2) + R(3) + R(4)), \qquad (4.1)$$

where *S* indicates the sky signal and *R* the reference signal, respectively. Dedicated *r*-values are calculated as

$$V_{out} = S(1) - r_1 \cdot R(2) + S(4) - r_2 \cdot R(3) + S(2) - r_3 \cdot R(1) + S(3) - r_4 \cdot R(4). \qquad (4.2)$$

In the dedicated method, separate *r*-values are used for different phase states of the same diode detector. The knee frequency with different *r*-values for each phase state is above 10 mHz with a temperature difference of 1.5 K between the signal and reference. Knee frequencies with "averaged" and dedicated *r*-values and single channel measurements are shown in Table 4.2. Three different phase switching frequencies were used in the measurements: 500 Hz, 250 Hz and 125 Hz. At a switching frequency of 125 Hz using the foxtrot method, the measured data was corrupted because of saturation in the back-end DC amplifiers.

Table 4.2. Comparison of knee frequencies (in mHz) when using different r calculations, different switching methods and different speeds.

Temperature difference [K]	f_k [mHz] single channel, optimum *r* (500Hz/250 Hz)	f_k [mHz] foxtrot, averaged *r* (500 Hz/250 Hz)	f_k foxtrot, [mHz] dedicated *r* (500 Hz/250 Hz)
-0.6	20 / 70	10 /30	<10 / 10
1.5	40	10	10
5.45	60	80	20
14.49	120	200	50

As shown in Table 4.2, the single channel and the averaged r-value give similar knee frequencies. The dedicated *r*-value is about 4 times better than that obtained using the other phase switching schemes. Unfortunately, the spacecraft onboard processing capability limits the phase switching to single channel.

4.3 Test setup and measurement of EBB receiver

The complete receiver measurement system monitors all the operational quantities and measures the required values with an adequate accuracy under simulated flight conditions. The bias and radiometer output voltages are easy to monitor and measure with high accuracy, while the cryogenic noise temperature measurements and FEM input reflections are the most difficult aspects.

The Cryogenic Microwave Test System (CMTS) was specifically built to test the Planck Satellite 70 GHz receiver. The CMTS consists of a stainless steel vacuum chamber with external dimensions of 1.6 x 1.0 x 0.3 m^3 and all required external electronics, a monitoring system, and measurement equipment. Different cryostat types were evaluated [51-58]; however, the requirements and the long testing time call for a more stable, easy-to-use testbed. It was decided that the cryogenic temperatures would be maintained using closed-cycle helium coolers (Advanced Research System Inc. DE-210 and APC-cryogenics Inc. CSW-204SL). The DE-210 two-stage cooler has a cooling power of 0.8W at the 4-K stage and 50 W at the 50-K stage. The CSW-204SL two-stage closed-cycle helium cooler has a cooling power of 9 W at 20 K and 15 W at 70 K. The first stages of the coolers are used to cool the radiation shield surrounding the FEM.

The vacuum was maintained by the Edwards E2B8 backing pump and the Edwards BRV25 diffusion pump. The vacuum was monitored by the Penning PR10-K sensor from $1 \cdot 10^{-4}$ mbar to $1 \cdot 10^{-9}$ mbar and by the Penning CP25-K sensor from 1 mbar to $1 \cdot 10^{-4}$ mbar. A vacuum of $1 \cdot 10^{-7}$ mbar was found to be achievable during measurements. A mass-spectrometer was also mounted on the chamber to monitor possible vacuum leaks. Leaks were monitored with helium gas from potential leakage points.

The ultra-low noise bias voltage supplies were made in house to be as close as possible to the $1\,\mu V/\sqrt{Hz}$ noise requirement. One bias supply provides the common drain voltage, two gate voltages and switched phase shifter voltages to one FEM ACA (two LNAs and phase shifter). For two FEM measurements, there were eight separate bias units. The LNA and phase shifter supplies were isolated, but the grounds are connected at the FEM as they are in the satellite. All the bias voltages and currents were monitored through a data acquisition switch unit (HP 34970A). A commercial power supply was used to generate the +/-5V voltages to BEM.

A Lake Shore 330 temperature controller and Lake Shore DT470 calibrated silicon diodes were selected for monitoring temperature at an accuracy of +/- 20 mK at 20 K.

Seven temperature diodes were connected to the cryogenic temperature, with one diode used for monitoring the BEM temperature. Several heater resistors were used to heat input signals, FEMs and the radiation shield. A Peltier element was used to stabilize the BEM temperature to required levels. The block diagram of the test system is shown in Figure 4.14.

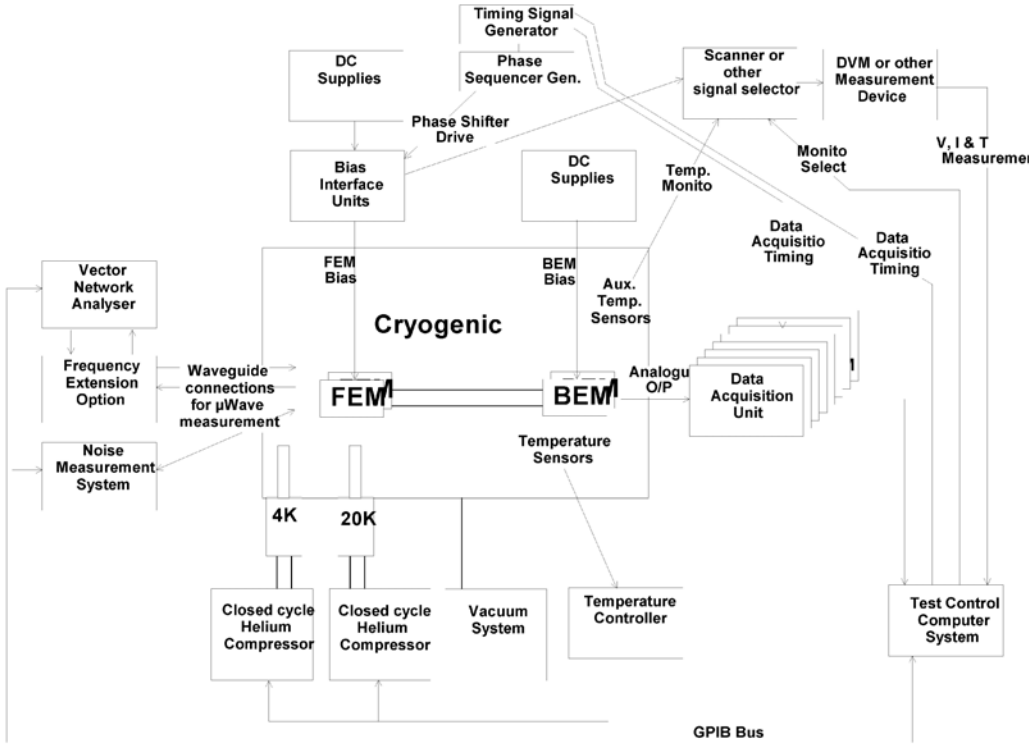

Figure 4.14. Block diagram of the test system for the complete receiver.

The Engineering Model (EM) receiver consists of two full FEMs and two full BEMs. For the FEM, four 25 dB Temperature Variable Attenuators (TVAs) were constructed to simulate the 4 K sky signal. The 4 K cold head cooling power limited the TVA temperature to 5-7 K. The gain and noise temperature of the FEM had to be measured separately in order to optimise the FEM bias voltages and operation of the radiometer. The 3 dB couplers (magic-Ts) were integrated into the FEM-BEM interconnecting waveguides to obtain intermediate output directly from the FEM. A three-dB coupler

was needed to attain enough power for the accurate noise and gain measurements. The vacuum chamber is shown in Figure 4.15.

a)

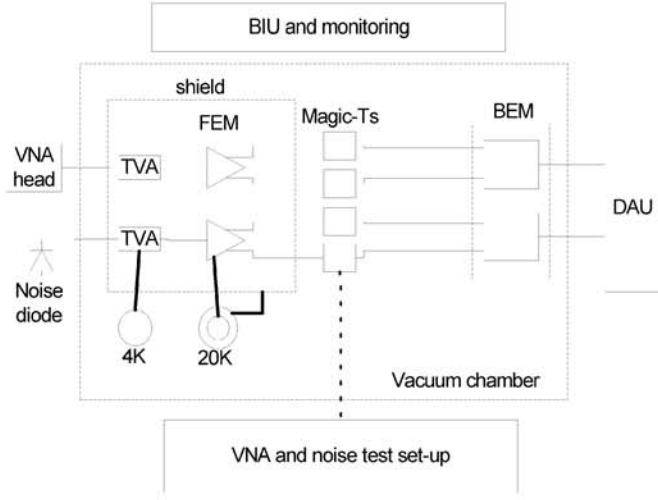

b)

Figure 4.15. a) The vacuum chamber for testing the Planck 70 GHz receiver with the EM waveguides. b) Block diagram of the test system for one receiver chain. The vacuum chamber and the external systems are designed for testing two receivers at the same time.

The back-end data acquisition system was designed to be similar to the spacecraft unit. The system consists of high linearity, low noise video amplifiers, analog integrate/reset and analog sample&hold circuits. From the sample&hold, the data was captured and passed to the AD converter. All systems were synchronised to one clock generator (Figure 4.16).

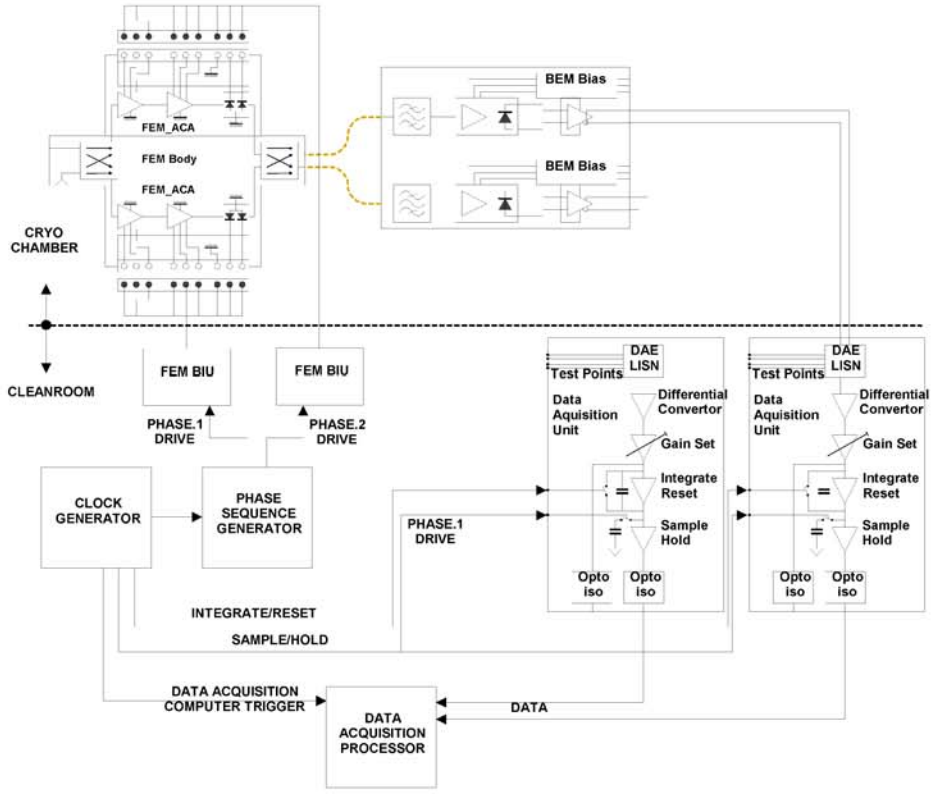

Figure 4.16. Data acquisition electronics block diagram.

4.3.1 Noise measurements

Radiometer sensitivity is the most critical parameter for a scientific mission [59-62]. Sensitivity is mainly determinated by the noise temperature of the receiver at a selected

integration time. Two separate methods were used to measure the noise of the receiver: heating the TVA from 5 K to 25 K and measurement with an externally calibrated noise diode. Single Side Band (SSB) total power was measured from the intermediate magic-T outputs. The power was measured both with 5 K physical temperature TVA and noise diode on and off and the same procedure was repeated with 25 K physical temperature TVAs. The TVAs had an adequate stabilization time of about 3 minutes. From available hot TVA and cold TVA output powers, the front-end system noise temperature T_{sys} was calculated with the Y-factor method. The noise diode was mostly used to optimise the receiver noise temperature. The noise measurement test system is shown in Figure 4.17.

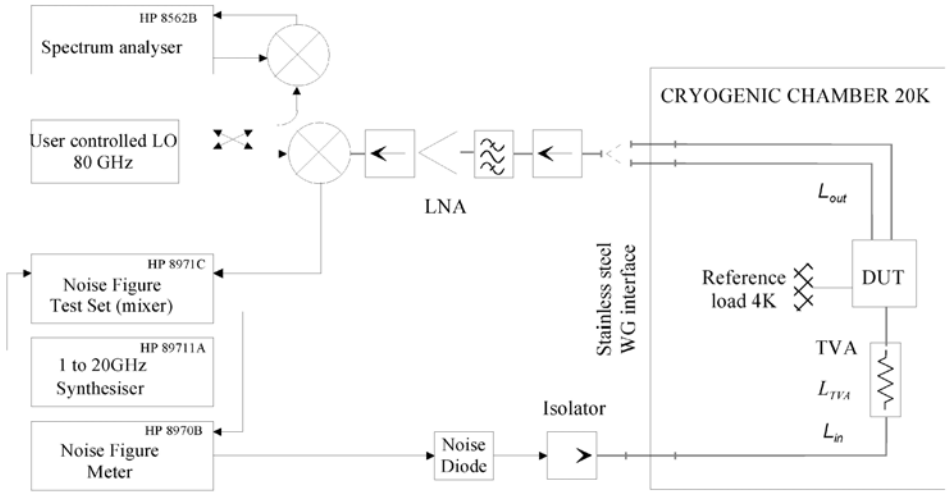

Figure 4.17. The noise test setup for one half of FEM measurements. The output from the chamber is the output of the magic-Ts. The second output passes to the BEM, and the third output is terminated with a load.

The noise receiver was a superheterodyne receiver with a 20 dB preamplifier. The first IF frequency band covers frequencies at 2-20 GHz. The first IF is fed to the noise figure test system (HP 8971C) for a second down conversion and single side band filtering. The total power was measured from the second 500 MHz IF signal. A spectrum analyzer (HP 8562B) was used to monitor the first LO frequency and relative power levels. The LO levels were tuned for the mixers optimum values. The noise temperature

of the noise receiver was measured using a microwave absorber immersed in liquid nitrogen during the noise diode calibration.

4.3.2 Noise measurement accuracy

Three different 25 dB TVAs were designed, measured and compared with noise diode measurements [63]. The measurement accuracy was estimated to be ±5 K using RSS and Monte-Carlo methods. The results measured using the noise diode and TVA agreed within the accuracy of the measurement. For the TVA and noise diode methods, the input losses and input match of the front-end module are the most critical aspects for accuracy [64–70].

The input waveguide temperature can be assumed to have temperature and loss distributions. Then, the DUT input noise temperature is [71]

$$T_x' = \frac{T_{NS}}{L_{in}L_{TVA}} + \frac{2}{L_{in}L_{TVA}}\int_0^l \alpha(z)T_l(z)L_z dz + T_{TVA}\left(1-\frac{1}{L_{TVA}}\right), \tag{4.3}$$

where T_{NS} is the noise diode temperature, $T_{\mathrm{NS}} \approx 295$ K, room temperature, when the noise diode is switched off and $290(10^{ENR/10} + 295/290)$ K when the noise diode is on; L_{TVA} is the attenuation of the TVA; and T_{TVA} is the physical temperature of the TVA. $\alpha(z)$ and $T_l(z)$ are the attenuation and temperature distributions along the waveguide.

The theoretical waveguide loss is given as $L = e^{\kappa\alpha l}$, where κ is a coefficient dependent on the surface roughness and oxidation of the waveguide inner walls, and l is the length of the waveguide. The values $\kappa = 3$ and $l = 107$ cm have been used. The attenuation constant of the waveguide is [72]

$$\alpha = \frac{R_s}{\eta\sqrt{1-(\lambda_0/2a)^2}}\left(\frac{1}{b}+\frac{{\lambda_0}^2}{2a^3}\right), \tag{4.4}$$

$\eta \approx 377\ \Omega$ is the free-space wave impedance, λ_0 is the free-space wavelength, and a and b are the waveguide dimensions. $R_s = \sqrt{\pi f \mu_0 / \rho_m}$ is the surface resistance, $\mu_0 = 4\pi \cdot 10^{-7}$ H/m the permeability of vacuum, and ρ_m is the resistivity of the waveguide material. The waveguide material resistivity depends on the temperature, and the values of $\rho_m = 5.7 \cdot 10^{-10}\ \Omega$m at 25 K, $\rho_m = 7.0 \cdot 10^{-9}\ \Omega$m at 150 K and $\rho_m = 1.7 \cdot 10^{-8}\ \Omega$m at 295 K are used. If $\alpha(z)$ and $T_l(z)$ are linearly distributed along the waveguide, the input noise temperature can be written as [71]

$$T'_x = \left[T_2 - \frac{T_1}{L_{in}} - \frac{2(T_2 - T_1)}{\sqrt{2(\lambda_2 - \lambda_1)}} \left(D\left(\frac{\lambda_2}{\sqrt{2(\lambda_2 - \lambda_1)}} \right) - \frac{1}{L_{in}} D\left(\frac{\lambda_1}{\sqrt{2(\lambda_2 - \lambda_1)}} \right) \right) + \frac{T_{NS}}{L_{in}} \right] \frac{1}{L_{TVA}} + T_{TVA}\left(1 - \frac{1}{L_{TVA}}\right), \quad (4.5)$$

where D is Dawson's integral over the waveguide length [73]. If an average temperature and loss values are used, the input noise temperature is

$$T_{h/c} = \frac{\frac{T_{NS}}{L_{WG}} + T_{WG}\left(1 - \frac{1}{L_{WG}}\right)}{L_{TVA}} + T_{TVA}\left(1 - \frac{1}{L_{TVA}}\right), \quad (4.6)$$

where T_{WG} is the measured average temperature of the input waveguides, and L_{WG} is input waveguide losses.

The input temperature error between averaged and linear distributions is less than 1K. For the noise diode measurements, the system noise temperature error is then less than 2K with averaged values. In the noise diode off measurements, the error between linear distribution and averaged temperature value is negligible. The averaged values are used to simplify the noise temperature calculations. Losses of the waveguides and the TVA are calibrated at 20 K by first replacing the DUT with a short-circuit block and the TVA with a stainless steel waveguide, and then measuring the input and output reflection losses. A straight-through waveguide is installed in place of the DUT, and the transmission loss is then measured. Finally, the TVA is installed and the transmission loss is measured.

Noise measurement accuracy was estimated by the Monte-Carlo method and the RSS method [74]. If the noise receiver noise temperature is ignored due to high (40 dB) FEM gain, the RSS uncertainty can be assumed to be:

$$\Delta T_{DUT} = \sqrt{\left(\frac{\partial T_{DUT}}{\partial T'_H}\Delta T'_H\right)^2 + \left(\frac{\partial T_{DUT}}{\partial T'_C}\Delta T'_C\right)^2 + \left(\frac{\partial T_{DUT}}{\partial Y}\Delta Y\right)^2}. \quad (4.7)$$

The uncertainty of the T'_x is calculated as the RSS of the parameters by partially differentiating the averaged input temperatures. The common equation for the $\Delta T'_x$ is

$$\Delta T'_x = \left[\left(\frac{\partial T'_x}{\partial T_{NS\_x}}\Delta T_{NS\_x}\right)^2 + \left(\frac{\partial T'_x}{\partial L_{in}}\Delta L_{in}\right)^2 + \left(\frac{\partial T'_x}{\partial T_{in}}\Delta T_{in}\right)^2 + \left(\frac{\partial T'_x}{\partial L_{TVA}}\Delta L_{TVA}\right)^2 + \left(\frac{\partial T'_x}{\partial T_{TVA}}\Delta T_{TVA}\right)^2\right]^{\frac{1}{2}}. \quad (4.8)$$

The typical values of the parameters used in the uncertainty calculations at 70 GHz are shown in Table 4.3.

Table 4.3. Typical measured values and estimated uncertainties for the cryogenic measurements.

parameter	**value**	**uncertainty**	**Unit**
L_{TVA}	27.8	0.1	dB
T_{TVA_H}	18.4	0.5	K
T_{TVA_C}	6.9	0.5	K
L_{in}	3.0	0.1	dB
T_{in}	150	10	K
T_{NS_C}	290	1	K
T'_H	18.7	0.5	K
T'_C	7.3	0.5	K
Y	0.5	0.1	dB

The noise measurement uncertainty for the TVA measurements calculated from the values in Table 4.3 gives less than ±5 K accuracy over the operational frequency band.

Input reflections of the DUT also constitute critical aspects for measuring amplifier noise. For this reason, the TVA is directly connected to the DUT. The TVA reflections are better than –25 dB at room temperature. The cryogenic reflection measurement was limited to –15 dB because of the mylar sheets in the WR-12 waveguide windows. That poor input match also passed on uncertainties to the noise measurements for the noise diode. Individual LNAs were separately measured on-wafer; a typical measurement result is shown in Figure 4.18.

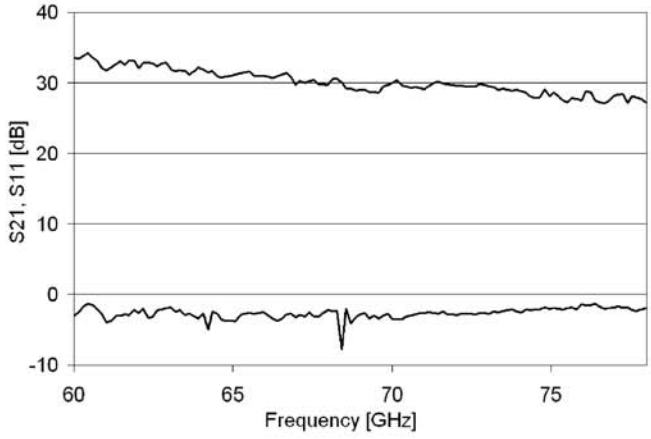

Figure 4.18. The S-parameters of an on-wafer LNA at a physical temperature of 20 K. V_d=0.7V, I_d=25mA.

Similar reflections were also measured for the EBB radiometer. If the effects of the measured reflections are removed from the noise temperature calculations, the noise temperature decreases by half. A typical noise temperature for the EM radiometer with and without the reflections is shown in Figure 4.19.

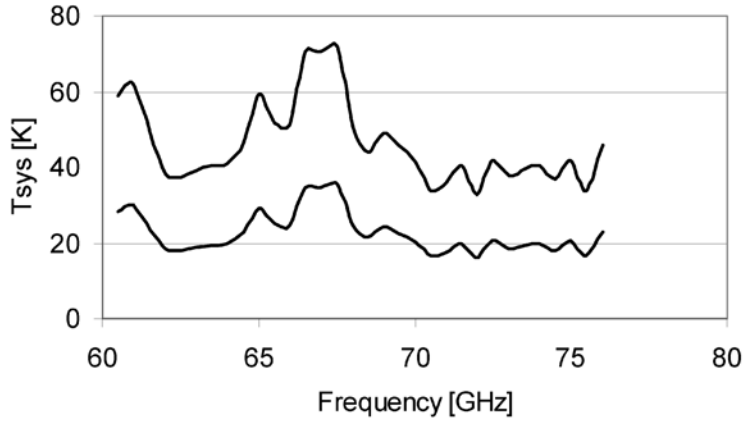

Figure 4.19. Typical T_{sys} of the EM radiometer measured with TVA. The upper curve is obtained without calculating the effect of the reflections, and the lower is the result after removing the effect of the mismatch.

The return loss requirement is 20 dB. This can be achieved with a proper waveguide to microstrip transition or by increasing the length of the other input waveguide by $\lambda/4$, which would in the ideal case cancel out the reflected waves at the FEM input waveguide interface. However, the latter solution does not reduce the receiver noise temperature.

4.3.3 FEM measurements

The VNA was calibrated outside the vacuum chamber with the normal TRL method. Typical calibration accuracy was measured to be +/- 0.02 dB in gain and +/- 0.5^{o} degrees in phase. All necessary external components, i.e., waveguides from the mm-wave head to DUT and the attenuators were measured individually at their normal operation temperatures.

The waveguides from the mm-wave heads to FEM were measured at 20 K under vacuum and during NTP operation. Input and output waveguide losses were measured with the reflection method using a waveguide short in the place of FEM. The reflection results were compared with the through measurement, and a good correlation was found between the two separate measurements. The through measurement was done with and

without TVA, thus allowing TVA loss to be calculated out from the results. The measured waveguide losses were removed from the FEM measurements externally. A block diagram of the gain and isolation measurement is shown in Figure 4.20.

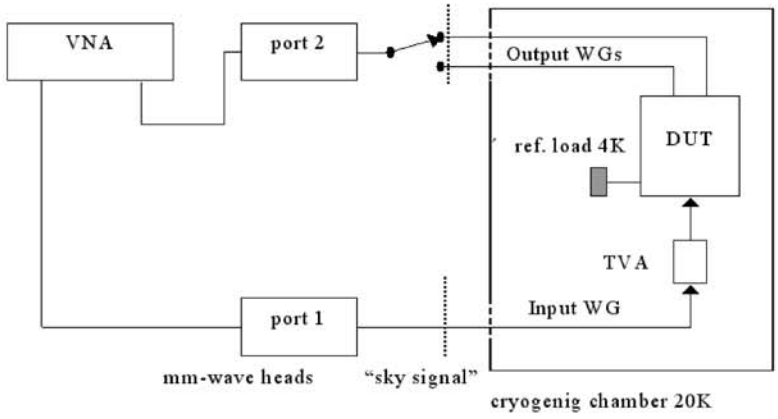

Figure 4.20. Block diagram of gain and isolation measurements. The calibration point is marked with a dotted line.

The typical gain of the FEM varied from 30 dB to 45 dB at different bias points. Normal isolation and gain are shown in Figure 4.21.

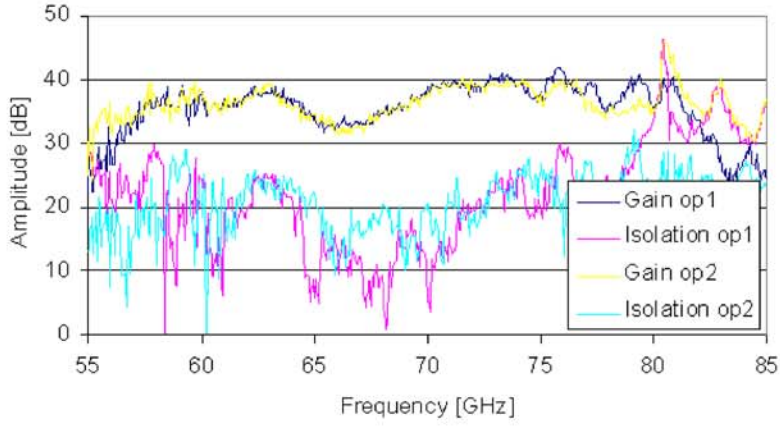

Figure 4.21. Typical FEM gain and isolation with ACA3 and ACA4.

A maximum gain of about 45 dB could be achieved with higher drain voltages, but the isolation was then only 5-10 dB. Minimum power consumption bias points were not documented because of poor (3-5dB) isolation, due to the totally different S_{21} performance between ACA3 and ACA4 with low power bias points.

The FEM noise temperature was measured always with the Y-factor method using two separate standards: the noise diode and a temperature variable attenuator (TVA). The TVA was found to be the most accurate way to measure cryogenic mm-wave amplifiers, although the noise diode is also accepted as a noise standard.

The TVA is based on wolfram-titanium plated 0.254 mm thick alumina vane. Overall, three different vane attenuators (W/Ti plated mica vane, W/Ti plated 0.1 mm alumina vane and W/Ti plated 0.254 mm alumina vane) were tested at cryogenic temperatures. The shape of the vanes was $\cos^2$ tapered to minimize reflections. The mica-based vane had the best reflection properties, while the 0.254 mm thick alumina had the smallest attenuation slope. Overall, the most repeatable noise results were measured with 0.254 mm thick W/Ti plated alumina vane. This is assumed to be due to thermal gradients in the vane, which are smallest in the 0.254 mm thick piece. A block diagram of the FEM noise measurement is shown in Figure 4.17. The noise source was the WR-12 noise source (Ylinen Ltd.) based on the Noise/Com W-band noise diode. The pass band back-end filter had a frequency band of 63-77 GHz. The external mixer was an ELVA BM-12-F. External mixer LO power and frequency were monitored with a spectrum analyzer and a harmonic mixer through a 25 dB multihole directional coupler.

The noise temperature of noise receiver was measured with liquid nitrogen and room temperature absorber using the WR-12 antenna as the input. The same measurement was repeated using a noise diode and a known room temperature attenuator as the noise source. The noise diode ENR value can be calibrated using the known noise temperature for the noise receiver. The noise temperature and calibrated ENR values for the noise receiver are shown in Figure 4.22.

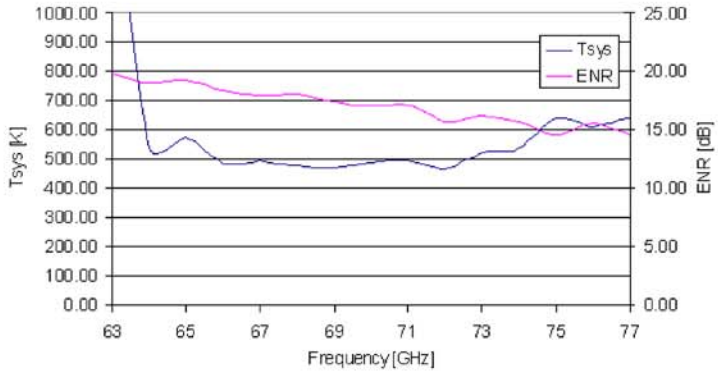

Figure 4.22. Noise receiver noise temperature and noise diode ENR values measured with liquid nitrogen and room temperature absorbers

Noise measurements were performed with the HP 8970B noise figure meter in total power mode using the 200 MHz IF-bandwidth. The input losses from the noise diode to DUT were removed with Friis' formulas. Optimum noise bias points were tuned with a calibrated noise test set and a noise diode, allowing the bias tuning to be performed real time without any external calculations. An EBB FEM noise optimized bias point noise response is shown in Figure 4.23.

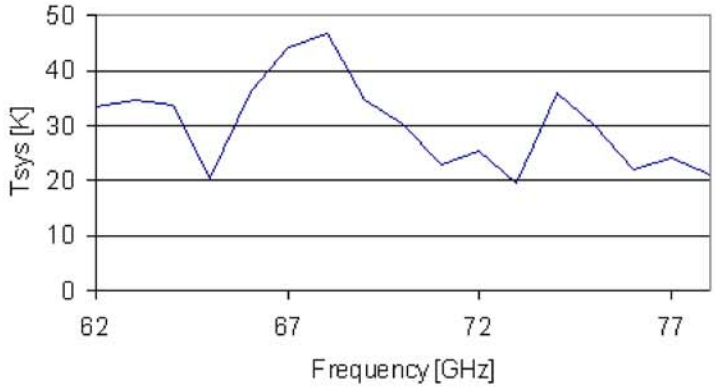

Figure 4.23. An EBB FEM noise response with optimum noise bias point using a noise diode as the noise source.

T_{sys} was always measured with the noise diode and the TVA. The results of the two different methods showed very good agreement. A normal T_{sys} difference between the TVA and externally calibrated noise diode measurements was +/- 5K. Figure 4.24 shows a typical measurement result. The high noise level is due to a broken LNA in ACA4.

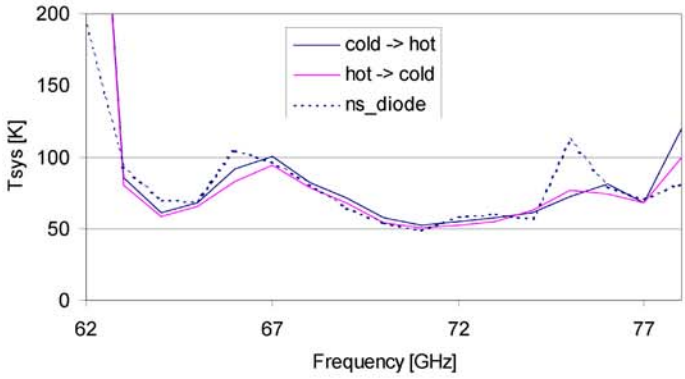

Figure 4.24. A normal noise response of FEM with broken LNA in ACA 4.

4.3.4 BEM measurements

BEM frequency response was measured using a known CW stimulus from the VNA and an HPIB controlled DVM. The measurement block diagram is shown in Figure 4.25.

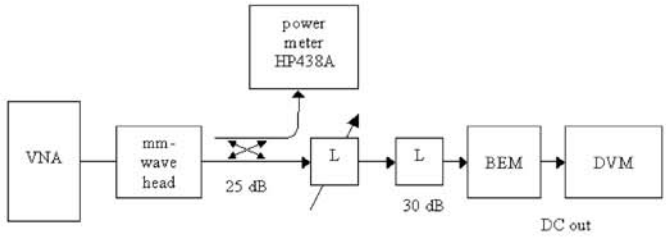

Figure 4.25. BEM frequency response and dynamic range measurement block diagram.

The HP 438A power meter was used to eliminate millimeter wave head power changes over the measured frequency bandwidth. The coupler losses and all the other known losses were eliminated with external calculations. The DVM used was a GPIB controlled FLUKE 8840A. A precision attenuator was tuned at 3 dB increments. The frequency responses of Channel 3 and Channel 4 with optimum gain bias points are shown in Figures 4.26 and 4.27.

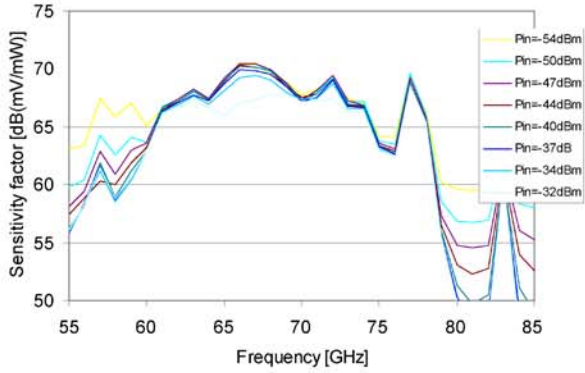

Figure 4.26. BEM Channel 3 sensitivity factor in dBs at optimum gain bias point.

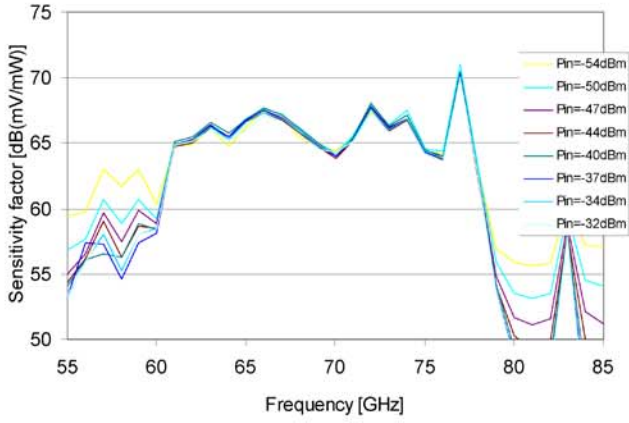

Figure 4.27. BEM Channel 4 sensitivity factor in dBs at the optimum gain bias point.

Optimum gain bias points are shown in Table 4.4. Monitored I_d values are for two parallel amplifiers, i.e., half BEM. The optimum gain bias point was adjusted individually for each channel. Video amplifier supply currents were monitored during measurements.

Table 4.4. BEM Channel 3 and 4 optimum gain bias points. I_d values for two parallel amplifiers.

	V_d [V]	V_g [V]	I_d [mA]	+V [V]	-V [V]	+I [mA]	-I [mA]	Power for ½ BEM [mW]
Ch3	0.678	0.155	47.83	5	-5	7.81	6.52	104.08
Ch4	0.651	0.206	63.65	5	-5	7.81	6.52	113.09

BEM frequency responses can be compared with individually measured BEM filters, as shown in Figure 4.28.

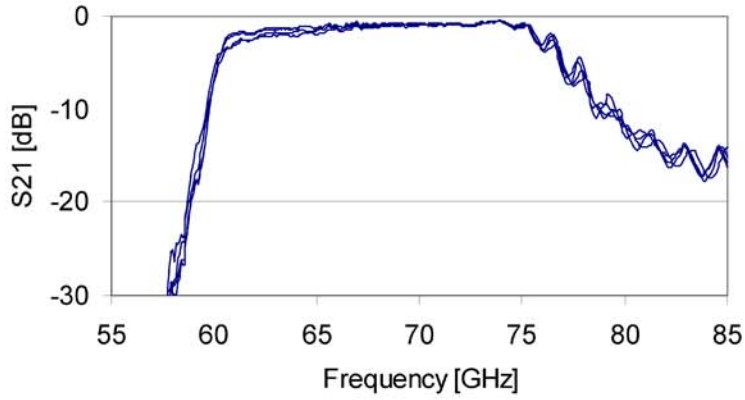

Figure 4.28. BEM filter frequency responses. The results include input and output copper waveguides about 5 cm in length.

The BEM filter pass band is slightly shifted towards lower frequencies but the shape and losses agree well with the simulated optimum case. The filter reflections were measured to be lower than -15 dB over their pass band.

BEM input reflections were measured directly with the VNA millimeter wave head using as low power as possible (lower than -20 dBm to prevent LNA saturation). The S_{11} is shown in Figure 4.29.

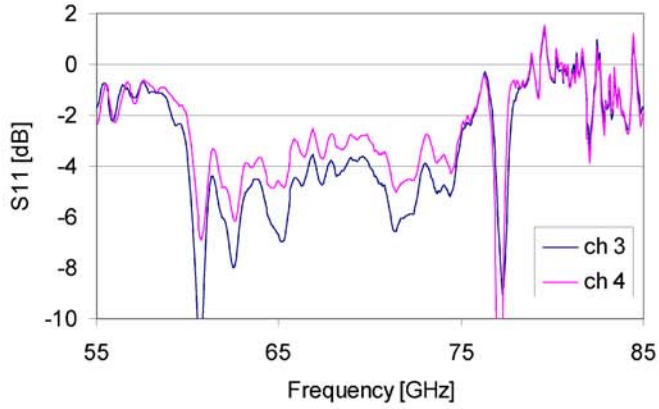

Figure 4.29. BEM S_{11}. Measured at NTP.

The BEM transient response was measured using a CW stimulus from the VNA and switching it on and off with external components. A block diagram of the transient response measurement is shown in Figure 4.30.

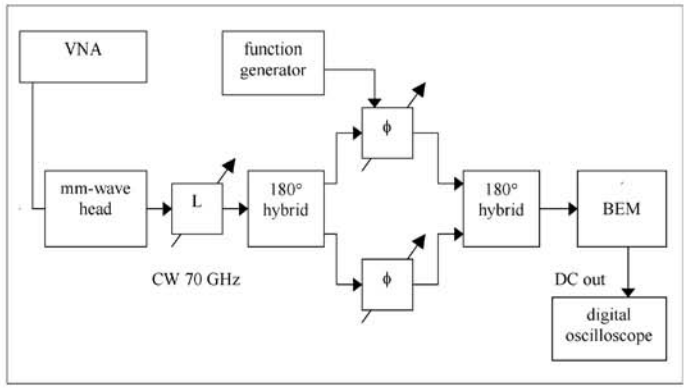

Figure 4.30. BEM transient response test setup.

A GW GFG-8015F function generator was used to control the 180° phase shifters with a rectangular wave. A Tektronix TDS 745 D 500 MHz digital oscilloscope was used to monitor the BEM output voltage. The phase shifters were Pacific mm-Product 6090m. The VNA was used in the CW mode at 70 GHz. The system was tested with ELVA-15 ZB detector diodes to have a rectangular output up to a sampling frequency of 20 kHz.

The input power was tuned to give about 2V BEM output voltage. At all tested frequencies, 63, 70 and 77 GHz, the BEM time constant was about 0.5 ms. Examples of measured oscilloscope signals are shown in Figure 4.31.

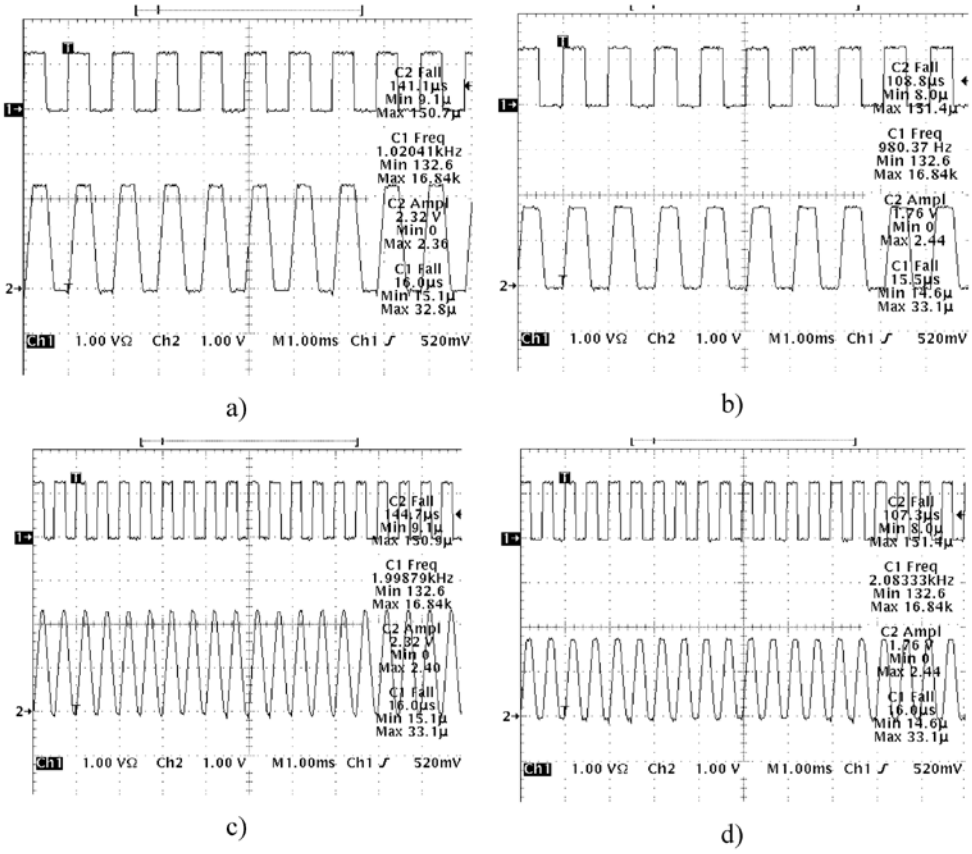

Figure 4.31. BEM transient response results. Lower curves show BEM output, while the upper denote the switching signals. a) Channel 3 with 1 kHz switching frequency, b) Channel 4 with 1 kHz switching frequency, c) Channel 3 with 2 kHz switching frequency and d) Channel 4 with 2 kHz switching frequency.

The long time constant was noted to be due to the BEM video amplifiers when they were measured individually. Because of limited test time, the video amplifiers were left in their original configuration (Figure 3.17). Individually packaged detector diodes were tested and found to have a time constant of less than 0.05 ms.

The BEM dynamic range was measured using the test setup shown in Figure 4.25 with a tunable precision attenuator. The attenuator was tuned to known attenuation values, and the frequency was swept while monitoring the output voltage with a DVM. When the

input power was tuned, the I_d value was monitored to detect possible LNA saturation. The frequency sweep was synchronized by PC. Channel 3 and Channel 4 dynamics at a frequency of 70 GHz are shown in Figure 4.32.

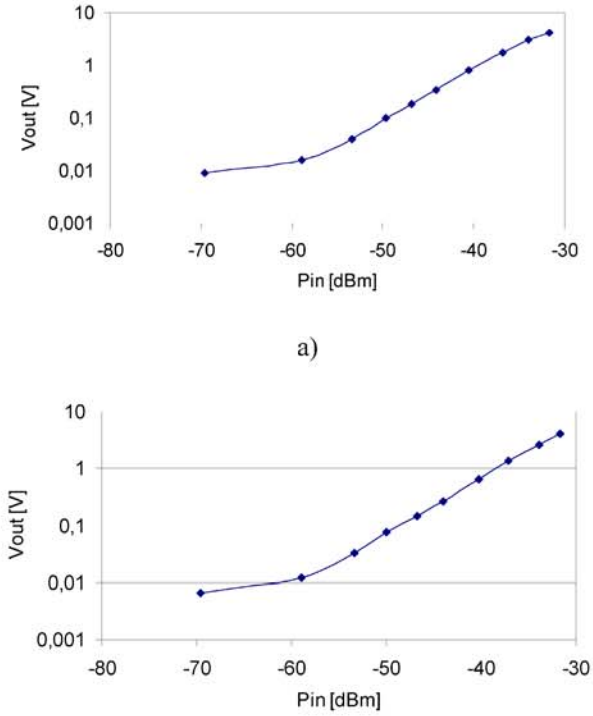

Figure 4.32. a) BEM Channel 3 and b) Channel 4 dynamic range with 70 GHz CW stimulus.

Both channels had a linear dynamic range from –54 dBm to –32 dBm that was limited by the 4 V output voltage of video amplifiers at various frequencies before any other saturation mechanisms. A typical P_{-1dBm} saturation power (output) for the room temperature LNA was measured to be about 0 dBm in the demonstrator phase of the Planck Project.

The BEM dynamic range was also measured with a wide band noise stimulus. The noise source and wide band LNA were used as the noise source and the amplitude was tuned with an adjustable attenuator as shown in Figure 4.33.

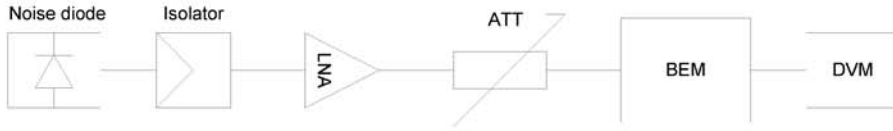

Figure 4.33. BEM dynamic range measurement block diagram when using wide band noise stimulus.

The results of the wide band noise stimulus results are shown in Figure 4.34.

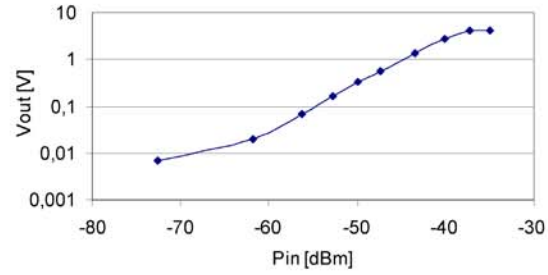

a)

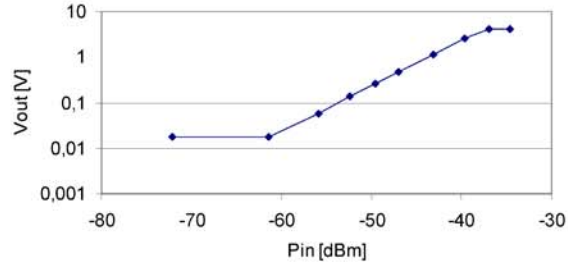

b)

Figure 4.34. a) BEM Channel 3 dynamic range with a wide band noise stimulus and b) BEM Channel 4 dynamic range with wide band noise stimulus. P_{in} is the power at the BEM input flange.

Input power was calculated using averaged noise diode ENT and averaged LNA noise and gain over an BEM input filter P_{-3dB} frequency range (61-77 GHz). As shown in Figures 4.34 a) and b), the BEM detector is operating in its square law region, and the BEM shows an approximately 20-dB dynamic range from –60 dBm to –40 dBm. The upper limit was again the video amplifier output voltage, thereby limiting the maximum voltage to 4 V. The difference between CW and noise stimulus dynamic range was caused by the filter slopes. The BEM noise temperature was measured to be about 1000 K.

4.4 EBB 1/*f*-noise measurements

Radiometer 1/*f*-noise was generated using cross-voltage over diodes with the "foxtrot" method. Half a second post integration time was used to generate low frequency PSDs. The "sky" signal had 8 K temperature variable attenuator as the signal source, while the reference horn was faced to a 5 K physical temperature load. Figure 4.35 shows the sky and the reference signals and foxtrot method differenced signal.

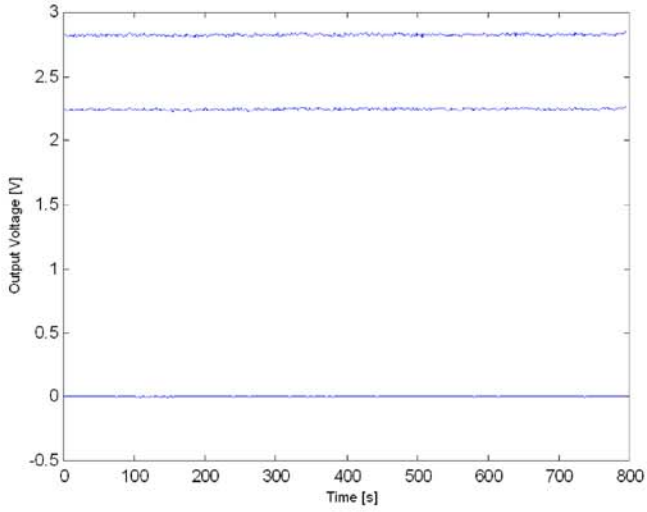

*Figure 4.35. 1/f-noise time based noise data. The upper line is "sky", middle line is the "reference" and the lowest line is the sky-r*ref using r=0.7945. The Y-axis is in volts, X-axis represents data points over 800 seconds.*

The phase switches were controlled with a 1 kHz signal. The optimized *r*-value was 0.7945. Figure 4.36 shows the generated PSDs on linear and logarithmic scales.

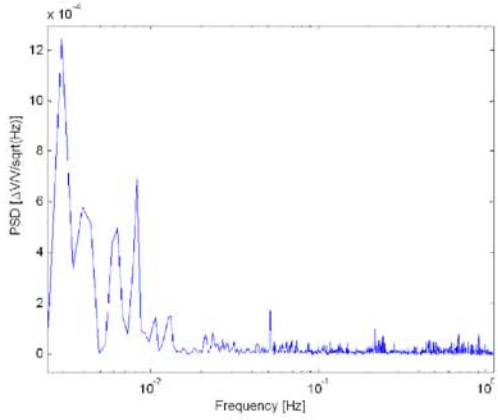

a)

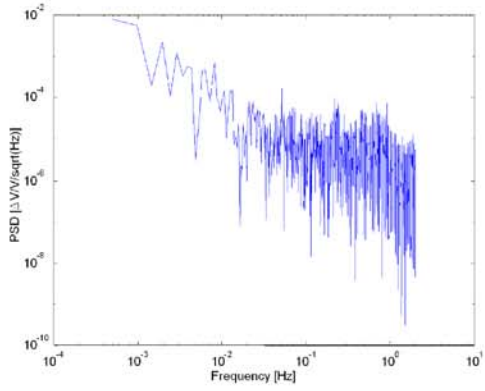

b)

Figure 4.36. EBB 1/f spectrums using the "foxtrot" sampling method. a) logarithmic x-axis and linear y-axis, b) logarithmic both axis. The r-value used was 0.7945.

An ideal ΔV/V noise level, $1.69 \cdot 10^{-5}$ (b=14 GHz, t=0.5), is reached at about 11 mHz. The ideal 14 GHz bandwidth used is larger because of the BEM filters which limit the operating frequency band to 61-77 GHz. Using 0.5 s post integration in the PSD generation, the white noise level (ΔV/V) is averaged to 1.26410^{-5}, i.e., an effective bandwidth of 17.7 GHz. The calculated effective bandwidth agrees with the measured BEM filter bandwidth.

The overall noise temperature was also calculated from known sky and reference load temperatures and the BEM output voltage using the Y-factor method. For radiometer noise, the hot temperature was reduced in the sky port of the FEM. The reduction was done with Friis' formulas using known TVA losses and known temperatures of the losses. The BEM output voltage was measured from both outputs with every phase switch state. The measured 4 K load temperature was used as the cold temperature. The phase switches were cotrolled at the 1 kHz frequency for 45 minutes. In Table 4.5, the voltages are the mean values over the 45-minute measurement period. The overall noise temperature can be calculated in the different phase switch positions using the measured voltages.

Table 4.5. Overall noise temperatures T_{sys} with all phase switch states.

Measured voltages				Y-values				Temperatures		Tsys	
op1	[V]	op2	[V]	op1		op2		Thot [K]	Tcold [K]	Op1 [K]	Op2 [K]
ph00	3.48	ph00	1.76	ph00/ph01	1.25	ph01/ph00	1.28	12.09	4.98	23.1	20.7
ph01	2.78	ph01	2.25	ph00/ph10	1.23	ph10/ph00	1.27	12.09	4.98	26.2	20.9
ph10	2.83	ph10	2.24	ph11/ph01	1.25	ph01/ph11	1.26	12.09	4.98	23.0	22.5
ph11	3.48	ph11	1.79	ph11/ph10	1.23	ph10/ph11	1.26	12.09	4.98	26.0	22.8

4.5 EBB summary

The required 35 dB gain and about 15 dB isolation were measured with the cooled (20 K) FEM. The performance of the noise temperature test setup for FEM measurements was improved with new TVAs. A minimum 20 K and an averaged 30 K FEM noise temperature over the required frequency bandwidth was measured with optimized ACAs.

The BEM frequency response was improved with a 3 dB attenuator between the BEM LNA and the detector. A conversion factor larger than $5 \cdot 10^7$ mV/mW was reached for overall BEM. The BEM dynamic range was limited by the video amplifiers to 4 V, and the BEM transient response time was also limited by the video amplifiers.

A conversion factor of about $1 \cdot 10^{10}$ mV/mW was measured for the total radiometer. The conversion factor response has a high ripple because of a gain dip in the FEM

performance. The total response flatness was not tuned to before knowing the “typical” ACA gain flatness. The response flatness can be tuned with bond wire stubs in the BEM input transitions or in the diode detector input. In addition, the detector design can be updated when the typical FEM gain values and BEM LNA gain values become known.

A 1/*f*-knee frequency of roughly 11 mHz was measured using the “foxtrot” sampling technique, and the radiometer noise temperature was measured to be 20 K, as found from 1/*f* measurement results. The overall FEM performance is repeatable and stable even with a “broken” LNA in ACA4.

The EBB gain, isolation and 1/*f* performance meet the flight requirements. Total radiometer sensitivity is good enough even if the conversion factor response has a high ripple. The ripple is due to the gain dip in the FEM. More “typical” ACA gain data is needed to finalize the BEM detector design in order to meet the total radiometer response flatness requirements. The operating radiometer meets EBB requirements for an integrated radiometer with sufficient performance. Table 4.6 shows the validation matrix for the 70 GHz EBB receiver.

Table 4.6. EBB receiver validation matrix

	Requirement	EBB receiver
Center frequency	70 GHz	69 GHz
Bandwidth (=20 %)	14 GHz	16.1 K
T_{sys}FEM+BEM	26 K	30-60 K
FEM gain	35 dB	35 dB
BEM RF gain	19 dB	20 dB
BEM DC gain	20 dB	20 dB
Video amp max. frequency	50 kHz	2 kHz
Tsys FEM	25.7 K	30-60 K
Tsys BEM	450 K	1000 K
Channel isolation	20 dB	15-20 dB
FEM gain flatness	+/- 1 dB	+/- 2.5 dB
BEM gain flatness	+/- 1 dB	+/- 2.5 dB
Overall gain flatness	+/- 1 dB	+/- 2.5 dB
1/*f*-knee frequency	50 mHz	<25 mHz
FEM power consumption	20.8 mW	24 mW
BEM power consumption	161 mW	400 mW
$\Delta T/T \cdot 10^6$, (t=0.5 s)	16.9	12.7

As shown in the validation matrix, the designed and validated receiver meets almost all of the requirements. The operational amplifier low pass filter can be adjusted to higher frequencies, although the selected OP27 amplifier limits the band to 30 kHz with a reasonable voltage gain. The gain flatness was also higher than desired, but the tuning was done after this thesis by adjusting the detector input impedance.

5 Summary of the publications

In paper [P1] developed the noise and gain cryogenic measurement setup for the individual V-band amplifiers as well as studied the behaviour of the amplifiers. For the continuous comparison receiver, the amplifiers must be phase, noise and gain matched in the pairs of parallel amplier chains. The effect of the bias point was studied to determine the best possible noise-gain-power parameters to meet the requirements for the complete receiver. The measurements were performed for the packaged MMICs because of the effect of waveguide on microstrip transitions.

Paper [P2] described the development of the 43 GHz astronomical receiver. The designed and constructed LNAs were based on the HRL InP-MMICs designed at the beginning of the Planck Project. The LNAs provided reasonably good gain and noise parameters, allowing them to be used in the 43 GHz amplifier design. The measured amplifiers showed very low noise (25K) at a temperature of 20 K. The amplifiers were noise optimized with the bias point at 20K.

Paper [P3] used an analytical approach to examine the theoretical susceptibility of the continuous comparator receivers to various systematic effects. In any CMB experiment, extracting the maximum information from the data requires efforts in understanding and minimizing systematic effects. This paper examined the effects of fluctuations in the amplifier gain, amplifier noise temperature, reference load temperature and the DC gain ratio, r. In addition, the effect of imperfect matching of amplifier gains and noise temperatures and of imperfect isolation between the sky and reference signals was analysed. Some simplifying assumptions were made in the analysis of the radiometer.

To verify the theory of the continuous comparator receiver concept, the demonstrator receiver was built and documented in paper [P4]. The receiver consists of selected NGST (formerly TRW) cryogenic InP-MMIC amplifiers cooled to a physical temperature of 20 K. The receiver was a combination of cooled and room temperature components because none of the phase shifter chips were good enough at that time. Moreover, the data collection unit and all electronics were developed for the

demonstrator receiver. Different phase switching schemes were studied based on the 1/*f* behaviour of the complete receiver. Partly based on this work, the final phase switching technique was selected for the flight model receivers.

Paper [P5] presented the measurements of the complete EBB model as well as a new cryogenic test setup for the FM receivers. The test setup consists of two coolers (4 K and 20 K), bias supplies, data collection units and a controlling PC. The coolers were installed into a large vacuum chamber where the complete receiver could be mounted. RF monitoring and testing was based on HP 8510 VNA as well as temperature variable attenuators as noise sources. Considerable effort was taken to improve the both reliability of the noise measurement as well as the noise level of the data collection unit. The measurement system was designed and built for a practical purpose: the receiver must have as many testing points as possible, and the tests must be measured between as many references as possible. For that reason, the temperature variable attenuators were selected in order to give hot and cold loads. The TVAs also allowed the noise diode to be used for minimizing the noise of the amplifiers as well as allowed the isolation to be measured with the VNA. In addition, the input noise temperature was reasonably low with 30 dB TVAs. Magic-Ts were mounted to enable possible measurement of the front-end module gain .

Paper [P6] described the design, building and measurements of a critical part of the continuous comparator receiver, the back-end module. In the back-end module, the frequency bandwidth is filtered using wide-band H-plane filters. After filtering, the signal is amplified 20 dB with LNA before detection and video amplification.

The complete EBB receiver was built and measured in paper [P7]. This publication finalizes the development of the EBB receiver. In the front-end module, the input waveguides from OMT and the reference load signals are combined in the magic-T. The combined signals are then amplified and phase switched in the parallel amplifier chains and then combined back to the original signals in the other magic-T. The front-end module is cooled to a physical temperature of 20 K, while the back-end module is at

room temperature. The measured results constituted the best published continuous comparator radiometer results at that time.

6 Discussion and conclusions

The purpose of this thesis was to develop instruments and verification setups for radioastronomical receivers and low noise amplifiers. The thesis has studied the noise measurement accuracy of the packaged amplifiers. This work has proven that the 1/*f*-noise reduction of a continuous comparator receiver works with cryogenic phase shifters at millimeter waves.

Chapter 2 outlined the theoretical background of the continuous comparator receivers and shows that it is possible to identify the most critical parameters of the receiver front-end. The *r*-value accuracy was found to be critical from the operational point of view. Comparing chapter 2 and paper [P3], susceptibilities of the continuous comparator receivers, the design aspects to the individual components of the receiver could be placed. In addition, it was possible to design the testing of the components based on the needed accuracies of individual components.

Several new amplifier and receiver designs were presented in Chapter 3. Our cryogenic LNAs include the design of all the required components: the MMIC chips, transitions, package and bias protections. Although design of the MMIC was not part of this thesis, part of the work was completed during this thesis. The WR-22 waveguide to microstrip transitions combined existing parts (K-pea) and novel design techniques. The 3D simulation of the amplifier package resonances was found to match with the measured values. The designed demonstrator receiver was the first cryogenic continuous comparator receiver at 70 GHz. In the EBB receiver, the phase switches were mounted for the first time in the cryogenic package with integrated magic-Ts and LNAs.

Chapter 4 showed that the “foxtrot” phase swiching method worked with cryogenic LNAs in the demonstator receiver. The continuous comparator receiver was improved for the first time using various r-value calculations (averaged and dedicated). A complete test setup was built for the cryogenic millimeter wave receiver. Improved noise measurement setups were built, and a comparison of different cryogenic Temperature Variable Loads (TVAs) was published. Extremely low receiver noise

temperatures were measured for the first time with a cryogenic continuous comparator receiver. The lowest 1/*f*-noise of the cryogenic continuous receiver was achieved with the demonstrator as well as with the integrated EBB receiver.

The measurement results shown in this thesis are from 2000-2004. After publishing the results, the Qualification Model (QM) and Flight Model (FM) receivers were built for the Planck satellite. The designed test systems with minor modifications were used in all the receiver tests. The complete receiver test system was used for over 3 years in the satellite tests after the publications included in this thesis. Additionally, our original FEM design was implemented in the real FM receivers. The BEM design was modified for the flight because of tightened volume and EMC specifications. The design updates were completed by the Finnish Planck team, mostly by Nicholas Hughes and Petri Jukkala at Ylinen Electronics.

In conclusion, this thesis presents the following new findings:

1. The feasibility of cryogenic millimeterwave LNAs has been demonstrated. The LNAs achieved the lowest known noise in the world measured at cryogenic temperatures within the operational frequency band.
2. Several cryogenic noise temperature measurement techniques have been studied at millimetre waves. Improved TVAs were developed for noise measurement.
3. An improved 1/*f*-noise cancellation method has been presented for the continuous comparator receiver.
4. A cryogenic V-band continuous comparator receiver has been built with integrated phase switches for the first time.
5. The lowest noise and 1/*f*-noise results have been presented for the V-band continuous comparator receiver.

References

[1] C.R. Lawrence, "*Bluebook-Planck, The Scientific Programme*", ESA-SCI(2005)1, www.rssd.esa.int/Planck/, Accessed Nov. 2008

[2] N. Mandolesi, C. Lawrence, M. Bersanelli, F. Pasian, C. Butler, "Planck LFI proposal executive summary", *Low frequency instrument for Planck, a proposal to the European Space Agency*, Feb. 16, 1998

[3] L. Valenziano, M. Sandri, G. Morgante, C. Burigana, M. Bersanelli, C. Butler, F. Cuttaia, F. Finelli, E. Franceschi, M. Galaverni, A. Gruppuso, M. Malaspina, N. Mandolesi, A. Mennella, F. Paci, L. Popa, P. Procopio, L. Stringhetti, L. Terenzi, M. Tomasi, F. Villa, J. Zuccarelli, "The low frequency instrument on-board the planck satellite: Characteristic and performance", *New Astronomy Reviews*, vol. 51, no. 3-4, pp. 287-297, 2007

[4] J.A. Tauber, "The Planck mission", *Advances in Space Research*, vol. 34, no. 3, pp. 491-496, 2004

[5] P. Kangaslahti, T. Gaier, D. Dawson, J. Tuovinen, T. Karttaavi, N.J. Hughes, T.L. Cong, P. Sjöman, S. Weinreb, "Low noise amplifiers in InP technology for pseudo correlating millimeter wave radiometer", *IEEE MTT-S 2001 International Microwave Symposium Digest*, vol. 3, pp. 1959-1962, 2001.

[6] J. Tuovinen, P. Kangaslahti, P. Haapanen, N. Hughes, P. Jukkala, T. Karttaavi, O. Koistinen, M. Lahdes, H. Salminen, J. Tanskanen, S. Urpo, "Development of 70 GHz receivers for the Planck LFI", *Astrophysical Letters and Communications*, vol. 37, pp. 181-187, 2000.

[7] D. Maino, C. Burigana, M. Maltoni, B.D. Wandelt, K.M. Gorski, M. Malaspina, M. Bersanelli, N. Mandolesi, A.J. Banday, E. Hivon,"The Planck-LFI instrument: Analysis of the 1/f noise and implications for the scanning strategy", *Astronomy and Astrophysics Supplement Series,* vol. 140, pp. 383-391, 2000

[8] M. Seiffert, A. Mennella, C.Burigana, N. Mandolesi, M. Bersanelli, P. Meinhold, P Lubin, "1/f- noise and other systematic effects in the Planck-LFI radiometers", *Astronomy and Astrophysics,* vol. 391, pp. 1185–1197, 2002

[9] D. Maino, C. Burigana, K.M. Gorski N. Mandolesi, M. Bersanelli, "Removing 1/f noise stripes in cosmic microwave background anisotropy observations", *Astronomy and Astrophysics*, vol. 387, pp. 356–365, 2002

[10] A. Mennella, M. Bersanelli, M. Seiffert, D. Kettle, N. Roddis, A. Wilkinson, P. Meinhold, "Offset balancing in pseudo-correlation radiometers for CMB measurements", *Astronomy and Astrophysics*, vol. 410, pp. 1089-1100, 2003

[11] A. Mennella, M. Bersanelli, C. Burigana, D. Maino, N. Mandolesi, G. Morgante, G. Stanghellini, "PLANCK: Systematic effect induced by periodic fluctuations of arbitrary shape", *Astronomy and Astrophysics*, vol. 384, pp. 736-742, 2002

[12] J. Protilla, E. Artal, E. Martinez-Gonzales, "Analysis of the 1/f-noise effects on the planck low-frequency instrument receivers", *Astrophysical Letters and Communications*, vol. 37, pp. 195-197, 2000

[13] M. Sandri, F. Villa, C. Burigana, A. Mennella, R. Nesti, N. Mandolesi, M. Bersanelli, "Straylight analysis and minimization strategy in PLANCK low frequency instrument", *Network Architectures, Management, and Applications II*, vol. 5962, pp. 575-586, 2005

[14] F. Cuttaia, P. Battaglia, L. Terenzi, C. Franceschet, M. Bersanelli, C. Burigana, C. Butler, O. D'Arcangelo, P. Guzzi, D. Maino, N. Mandolesi, A. Mennella, G. Morgante, A. Simonetto, L. Valenziano, F. Villa, "Analysis of the pseudocorrelation radiometers for the low frequency instrument onboard the PLANCK satellite", *Millimeter and Submillimeter Detectors for Astronomy II*, vol. 5498, pp. 756-767, 2004

[15] A. Mennella, M. Bersanelli, C. Burigana, D. Maino, R. Ferretti, G. Morgante, M. Prina, N. Mandolesi, C. Butler, L.Valenziano, F. Villa, "Analysis of thermally-induced effects in Planck Low Frequency Instrument", *American Institute of Physics Conference Proceedings*, vol. 616, pp. 229-233, 2002

[16] A. Mennella, M. Bersanelli, R.C. Butler, D. Maino, N. Mandolesi, G. Morgante, L. Valenziano, F.Villa, T. Gaier, M. Seiffert, S. Levin, C. Lawrence, P. Meinhold, P. Lubin, J. Tuovinen, J. Varis, T.Karttaavi, N. Hughes, P. Jukkala, P. Sjöman, P. Kangaslahti, N. Roddis, D., Kettle, F. Winder, E. Blackhurst, R. Davis, A. Wilkinson, C. Castelli, B. Aja, E. Artal, L. de la Fuente, A. Mediavilla, J.P. Pascual, J. Gallegos, E. Martinez-Gonzalez, P. de Paco, L. Pradell, "Advanced pseudo-correlation radiometers for the Planck-LFI I instruments", *Proc. 3rd ESA Workshop on Millimetre Wave Technology and Applications*, pp. 69-75, Espoo, 2003

[17] M.W. Pospieszalski, J.W. Edward, "Characterictics of broadband InP HFET millimeter-wave amplifiers and their applications in radio astronomy receivers", *Topical Symposium on Millimeter Waves,* vol. 7, pp. 143-146, 1997

[18] A. Cappy, "Noise modelling and measurement techniques", *IEEE Transactions on Microwave Theory and Techniques,* vol. 36, pp. 1-10, 1988

[19] M.W. Pospiezalski, "Modeling noise parameters of the MESFET's and MODFET's and their frequency and temperature dependence", *IEEE Transactions on Microwave Theory and Techniques,* vol. 37, pp. 1340-1350, 1989

[20] N.C. Jarosic, "Measurements of the low-frequency-gain fluctuations of a 30-GHz high-electron-mobility-transistor cryogenic amplifier", *IEEE Transactions on Microwave Theory and Techniques*, vol. 44, no. 2, pp. 193-197, 1996

[21] E.J. Wollack, "High-electro-mobility-transistor gain stability and its design implications for wide band millimeter wave receivers", *Review of Scientific Instruments,* vol. 66, pp. 4305-4312, 1995

[22] E.J. Wollack, M.W. Pospieszalski, "Characteristics of broadband InP millimeter-wave amplifiers for radiometry", *IEEE MTT-S 1998 International Microwave Symposium Digest*, vol. 2, pp. 669-672, 1998

[23] J.D. Gallego, I.L. Fernández, "Measurements of gain fluctuations in GaAs and InP cryogenic HEMT amplifiers", *Technical Report: Centro Astronomico de Yebes*, pp. 1-6, 2000.

[24] D.H. Je, S.T. Han, T.S. Kim, H.J. Kim, K.D. Kim, M.H. Chung, C.H. Lee, D.G. Roh, "The development of Q-band HEMT receiver for VLBI", *Journal of Astronomy and Space Science*, vol. 21, pp. 29-38, 2004

[25] J. Tanskanen, P. Kangaslahti, H. Ahtola, P. Jukkala, T. Karttaavi, M.Lahdes, J. Varis, J. Tuovinen, "Cryogenic indium-phosphide HEMT low-noise amplifiers at V-band", *IEEE Transactions on Microwave Theory and Techniques*, vol. 48, pp. 1283-1286, 2000

[26] C. Yang, B. Nelson, B. Allen, W. Jones, B. Horton, "Cryogenic characteristics of wide-band pseudomorphic HEMT MMIC low-noise amplifiers", *IEEE Transactions on Microwave Theory and Techniques*, vol. 41, no. 6, pp. 992-997, 1993

[27] T. Saito, Y. Oohashi, H. Kurihara, Y. Hirachi, T. Kasuga, K. Miyazawa, "A cryogenic 43-GHz-band low-noise amplifier for radio astronomy", *IEEE MTT-S 1989 International Microwave Symposium Digest*, vol. 3, pp. 853-856, 1989

[28] H. Wang, R. Lai, Y. Kok, T. Huang, M. Aust, Y. Chen, P. Siegel, T. Gaier, R. Dengler, B. Allen, "A 155-GHz monolithic low-noise amplifier", *IEEE Transactions on Microwave Theory and Techniques*, vol. 46, no. 11, pp. 1660-1666, 1998

[29] M.W. Pospiezalski, W.J. Lakatosh, E. Wollack, L.D. Nguyen, L. Minh M. Lui, L. Takyiu, "Millimeter-wave waveguide-bandwidth cryogenically-coolable InP HEMT amplifiers", *IEEE MTT-S 1997 International Microwave Symposium Digest*, vol. 3, pp. 1285–1288, 1997

[30] M.W. Pospiezalski, E. Wollack, N. Bailey, D. Thacker, J. Webber, L.D. Nguyen, M. Lem, M. Lui, "Design and performance of wideband, low-noise, millimeter-wave amplifiers for microwave anisotropy probe radiometers", *Radio Frequency Integrated Circuits (RFIC) Symposium Digest*, pp. 217-220, 2000

[31] M.W. Pospiezalski, E. Wollack, "Ultra-low-noise InP field effect transistor radio astronomy receivers: State-of-the-art", *Microwaves, Radar and Wireless Communications*, vol. 3, pp. 23-32, 2000

[32] M.W. Pospieszalski, S. Weinreb, R. Norrod, R. Harris, "FET's and HEMT's at cryogenic temperatures-their properties and use in low-noise amplifiers", *IEEE Transactions on Microwave Theory and Techniques*, vol. 36, no. 3, pp. 552-560, 1988

[33] N. Jarosik, "The use of cryogenic HEMT amplifiers in wide band radiometers", *Gallium Arsenide Applications Symposium, GAAS 2000*, pp. 1-4, 2000

[34] K.H.G. Dub, P.C. Chao, P.M.Smith, L.F. Lester, B.R.Lee, J.M. Ballingall, M.Y. Kao, "Millimeter-wave low-noise HEMT amplifiers", *IEEE MTT-S 1988 International Microwave Symposium Digest*, vol. 2, pp. 923-926, 1988

[36] S. Weinreb, R. Harris, M. Rothman, "Millimeter-wave noise parameters of high performance HEMT's at 300 K and 17 K", *IEEE MTT-S 1989 International Microwave Symposium Digest*, vol. 13, pp. 813-816, 1989

[37] M.W. Pospieszalski, W.J. Lakatosh, "Millimeter-wave, cryogenically-coolable amplifiers using AIInAs/GaAnAs/InP HEMTs," *IEEE MTT-S 1993 International Microwave Symposium Digest*, vol. 2, pp. 515-518, 1993

[38] Y. Hirachi, S. Kuroda, "Status of millimeter-wave MMIC's and their applications in Japan", *European Microwave Conference*, pp.1-4, 2000

[39] K.H.G. Dub, P.C. Chao, S. Liu, P. Ho, M. Kao, J. Ballingall, "A super low-noise 0.1 μm T-gate InAIAs-InGaAs-InP HEMT" *IEEE Microwave and Guided Wave Letters*, vol. 1, no. 5, pp. 114-116, 1991

[40] P.D. Chow, K. Tan, D. Streit, D. Garske, P. Liu, R. Lai, "W- and D-band low noise amplifiers using 0.1 micron pseudomorphic lnAIAs/lnGaAs/lnP HEMTs", *IEEE MTT-S 1992 International Microwave Symposium Digest*, vol. 2, pp. 807-810, 1992

[41] N.G. Lai, Y. Hwang, H. Wang, D.C.W. Lo, T. Block, K. Tan, D.C. Streit, R. Dia, A. Freudenthal, P.D. Chow, J.Berenz, "A fully passivated ultra low noise W-band monolithic lnGaAs/lnAIAs/lnP HEMT amplifier", *IEEE Microwave and Millimeter-Wave Monolithic Circuits Symposium*, vol. 15, pp. 63-66, 1995

[42] Y.C. Leong, S. Weinreb, "Full band waveguide-to-microstrip probe transitions", *IEEE MTT-S 1999 International Microwave Symposium Digest* vol. 4, pp. 1435-1438, 1999

[43] F. Villa, M. Sandri, M. Bersanelli, C. Butler, N. Mandolesi, A. Mennella, J. Marti-Canales, J. Tauber, "Planck / Lfi: An advanced multi-beam high performance mm-wave optics for space applications", *Proceedings of the 25 Antenna Workshop on Satellite Antenna Technology*, 2002

[44] N. Marcuvitz, "*Waveguide Handbook"*, Dover Publications, 1965

[45] G. Matthaei, L. Young, E.M.T. Jones, "*Microwave Filters, Impedance-Matching Networks, and Coupling Structures"*, Artech House, 1964

[46] A.R. Thompson, D.T. Emerson, "Relative sensitivity of full-wave and half-wave detectors in radio astronomy", *Radio Science*, vol. 38, pp. 1-16, 2003

[47] J.R. Cogdell, S. Wu-Hung,"Effects of video detector saturation on radiometer linearity", *IEEE Transactions on Microwave Theory and Techniques*, vol. 18, no. 6, pp. 324-325, 1970

[48] http://www.analog.com/UploadedFiles/Data_Sheets/OP27.pdf, Accessed Nov. 2008

[49] P.F. Muciaccia, M. Bersanelli, P. Bernardis, N. Vittorio, S. Masi, N. Mandolesi, "Sub-degree CMB anisotropy from space I. Sky coverage and sensitivity", *Astronomy and Astrophysics*, vol. 117, pp. 569-582, 1996

[50] Y.T. Chan, Q. Ma, H.C. So, R. Inkol, "Evaluation of various FFT methods for single tone detection andfrequency estimation", *IEEE Canadian Conference on Electrical ad Computer Engineering*, vol. 1, pp. 211-214, 1997

[51] N. Delruelle, F. Haug, H. Ten, "The helium cryogenic system for the ATLAS experiments", *IEEE Transactions on Applied Superconductivity*, vol. 10, pp. 1511-1513, 2000

[52] F. Haug, A. Cambon N. Delruelle, J.P. Orlic, G. Passardi, J. Tischhauser, "The CERN cryogenic test facility for the Atlas barrel toroid magnets*", IEEE Transactions on Applied Superconductivity*, vol. 10, pp. 1514-1517, 2000

[53] D.G. Akopjan, A.N. Bondarchuk, V.N. Vasiljev, A.M. Dedurin, V.V. Kalinin, V.A. Karnaukh, V.E. Korsunsky, A.I. Kostenko, G.V. Trokhachev, V.V. Filatov, O.G. Filatov, R.V. Chvartatsky, A.T. Chegodaev, "Facility for electrical and mechanical tests at cryogenic temperature", *IEEE Transactions on Magnetics*, sol. 28, pp. 613-615, 1992

[54] C. Reese, J. Susta, T. Powers, B. Almeida, "A closed cycle cryogenic system for testing superconductive RF cavities", *IEEE Particle Accelerator Conference*, vol. 4, pp. 2325-2327, 1991

[55] V. Glukhink, O. Filatov, V. Belyakov, S. Egorov, V. Korsunsky, I. Rodin, "Cryogenic test facility of the D.V. Efremov institute", *IEEE Transactions on Applied Superconductivity*, vol. 10, pp. 1564-1567, 2000

[56] R. Bourque, M. Wykes, "The ITER cryostat", *16th IEEE/NPSS Symposium Publication*, vol. 1, pp. 353-356, 1995

[57] R. Ross, "JPL Cryocooler development and test program: A 10-year Overview", *IEEE Aerospace Conference*, vol. 2, pp. 115-124, 1999

[58] G. Behrens, W. Campbell, D. Williams, S. White, "*Guidelines for the Design of the Cryogenic Systems*", *NRAO Electronics Division Internal Report*, no. 306, 1997

[59] C. Burigana, D. Maino, K. Gorski, N. Mandolesi, M. Bersanelli, F. Villa, L. Valenziano, B. Wandelt, M. Maltoni, E. Hivon, "PLANCK LFI: Comparison between galaxy straylight contamination and other systematic effects", *Astronomy & Astrophysics*, vol. 373, pp. 345-358, 2001

[60] P. Muciaccia, M. Bersanelli, P. Bernardis, N. Vittorio, S. Masi, N. Mandolesi, "Sub-degree CMB anisotropy from space, sky coverage and sensitivity", *Astronomy & Astrophysics Supplement Series*, vol. 117, pp. 569-582, 1996

[61] M. Maris, D. Maino, C. Birigana, A. Mennella, M. Bersanelli, F. Pasian, "The effect of the signal digisation in CMB experiments", *Astronomy and Astrophysics*, vol. 414, pp. 777-794, 2004

[62] M. Bersanelli, P. Muciaccia, P. Natoli, N. Vittorio, N. Mandolesi, "Sub-degree CMB anisotropy from space, in-flight calibration", *Astronomy and Astrophysics Supplement Series*, vol. 121, pp. 393-404, 1997

[63] P. Sjöman, S. Ovaska, P. Jukkala, N. Hughes, P. Eskelinen, S. Urpo, "V-band cryogenic attenuators for cryogenic noise measurements", *URSI/IEEE XXVII Convention on Radio Science,* pp. 198-200, 2002.

[64] D.F. Wait, T. Nemoto, "Measurement of the noise temperature of a mismatched noise source*", IEEE Transactions on Microwave Theory and Techniques*, vol. 16, no. 9, pp. 670-675, 1968

[65] G.L. Williams, "A broadband radiometer for calibration mismatched noise sources", *Conference on Precision Electromagnetic Measurements,* vol. 1, pp. 30-31, 1990

[66] D.F. Wait, "Thermal noise from a passive linear multiport", *IEEE Transactions on Microwave Theory and Techniques*, vol. 16, pp. 687-691, 1968

[67] T. Nemoto, D.F. Wait, "Microwave circuit analysis using the equivalent generator concept", *IEEE Transactions on Microwave Theory and Techniques,* vol. 16, pp. 866-873, 1968

[68] D.F. Wait, "The precision measurement of noise temperature of mismatched noise generators", *IEEE Transactions on Microwave Theory and Techniques,* vol. 18, pp. 715-724, 1970

[69] T. Otoshi, "The effect of mismatched components on microwave noise-temperature calibrations", *IEEE Transactions on Microwave Theory and Techniques,* vol. 16, pp. 675-686, 1968

[70] W.R. McGrath, A.V. Räisänen, P.L. Richards, "Variable temperature loads for use in accurate noise measurements of cryogenically-cooled microwave amplifier and mixers", *International Journal of Infrared and Millimeter Waves*, vol. 7, no. 4, pp. 543-553, 1986

[71] C. T. Stelzried, "Microwave thermal noise standards", *IEEE Transactions on Microwave Theory and Techniques,* vol. 16, no. 9, pp. 646-655, 1968.

[72] A. Lehto, A. Räisänen, "*Mikroaaltomittaustekniikka",* Otatieto, Helsinki, 1999

[73] M. Abramowitz, I.A. Stegun, "*Handbook of Mathematical Functions",* Dover Publications Inc, New York, 1972

[74] J. Mallat, R. Leppänen, A. Räisänen, "Study on the measurement uncertainty of noise properties of a millimeter wave amplifier", *Helsinki University of Technology, Radio Laboratory*, Report S-200, Espoo, 1993

Reprints of publications P1 to P7

ISBN 978-951-22-9747-4
ISBN 978-951-22-9748-1 (PDF)
ISSN 1795-2239
ISSN 1795-4584 (PDF)